scientific reports

Check for updates

OPEN

Combining deep learning and microfluidics for fast and noninvasive sorting of zebrafish embryo

Alioune Diouf[1,2]✉, Ferhat Sadak[3], Leandre Bereziat[1], Edison Gerena[1], Florian Fage[1], Abdelkrim Mannioui[5], Daniela Zizioli[6], Irene Fassi[4], Mokrane Boudaoud[1], Giovanni Legnani[2] & Sinan Haliyo[1]

Sorting of zebrafish embryos remains a challenging task in biomedical research. There is a need for accurate and efficient methods to distinguish between embryos at *Stage 1*, the zygote period immediately after fertilization, characterized by the single-cell stage, as well as those at advanced developmental stages (above single-cell stage) and non-viable (*Dead*) embryos. Manual sorting is labor-intensive, error-prone, and time-consuming. Traditional automated techniques, such as fluorescence-activated cell sorting (FACS) and robotic systems, are often invasive or prohibitively expensive, limiting their accessibility and scalability for routine zebrafish embryo sorting. This paper presents a novel approach that integrates deep learning with microfluidic technology to address these limitations. Our system utilizes a YOLOv8-based deep learning model for real-time embryo classification, whereas a microfluidic chip which is equipped with peristaltic pumps, ensures precise sorting with minimal manual intervention. Computational Fluid Dynamics (CFD) simulations are performed to optimise the flow parameters, and experimental validation demonstrate the system's high accuracy and sorting efficiency. The YOLOv8 model demonstrate a detection accuracy of 97.6 % and a processing speed of 10.5 ms. The sorting experiments demonstrate the system's efficacy, with the *Stage 1* class achieving a detection accuracy of 90.63 % and a sorting efficiency of 88.13 %. The *Advanced* class exhibited enhanced performance, with a detection accuracy of 93.36 % and a sorting efficiency of 91.80 %. The *Dead* class demonstrate the highest performance, with a detection accuracy of 99.03 % and a sorting efficiency of 96.60 %. The system demonstrate an average sorting rate of 2.92 s per embryo. This approach provides a reliable, cost-effective alternative to traditional methods, significantly improving the speed and precision of embryo sorting.

The zebrafish (*Danio rerio*) is an important model organism for the study of developmental genetics and the discovery of new drugs[1–4]. The use of the zebrafish has resulted in notable advancements in various medical fields, including hematopoietic[5,6], cardiovascular and vascular disorders[7–9]. Zebrafish mutants are used to investigate a range of diseases, including tumors and neurodegenerative disorders such as Alzheimer's disease[10,11] and Huntington's disease[12–14]. They also help investigate neuromuscular diseases, including Duchenne muscular dystrophy[15,16]. Consequently, zebrafish represent an exceptional model for studying human diseases, with 80% of their genes shared with humans[17]. However, sorting of zebrafish embryos is critical for ensuring experimental precision and reproducibility.

In the context of drug screening applications, embryo sorting techniques ensure uniformity and viability. The process of sorting eliminates nonviable or unfertilised embryos, preventing contamination. This improves the reliability of high-throughput tests for drug efficacy or toxicity[18]. Early embryo separation prevents cross-contamination and excludes irrelevant samples, ensuring research reliability. The sorting of embryos at specific developmental stages allows researchers to obtain standardised samples, which is crucial for accurate

[1]Sorbonne Université, Institut des Systèmes Intelligents et de Robotique (ISIR), Paris 75005, France. [2]Universita degli Studi di Brescia, Department of Industrial Engineering, Brescia, Italy. [3]Bartin University, Department of Mechanical Engineering, Bartin 74110, Türkiye. [4]Institute of Intelligent Industrial Technologies and Systems for Advanced Manufacturing National Research Council of Italy, Milan, Italy. [5]Sorbonne Université, Institut de Biologie Paris-Seine (IBPS), Paris, France. [6]Universita degli Studi di Brescia, Department of Molecular and Translational Medicine, Brescia, Italy. ✉email: diouf@isir.upmc.fr

comparisons, particularly in studies of gene expression and organ formation[19]. This approach eliminates variability caused by differences in development timing, thereby improving the reliability of the results[20]. However, manually handling zebrafish embryos is a time-intensive and tedious task because of their small size and large number of samples needed for experiments[21]. For example, manually positioning embryos into 96-well plates requires two skilled technicians for approximately three hours to fill 30 plates, with an avereage of 12 minutes per plate. This labor-intensive process is prone to errors and is physically demanding, limiting single technicians to three-hour sessions[22].

Automated systems offer faster, more accurate, and consistent sorting, significantly improving productivity and experimental precision in zebrafish research. Image-based cell sorting (IBCS) techniques combine high-content imaging with computational analyses, offering detailed visual insights into individual cells and enabling the development of advanced sorting criteria for improved classification accuracy[23]. Deep learning (DL) enhances detection by automatically learning features from complex, high-dimensional data, making it an indispensable tool for image recognition, object detection, and classification in biological research. The integration of deep learning with robotic automation has the potential to transform biological research, enabling faster and more precise workflows, such as high-throughput screening and automated sorting.

Several software algorithms, including YOLO[24] and Inception networks[25], have achieved classification accuracies exceeding 90% for zebrafish embryos by recognising distinct image features. Further advancements by Alegria et al.[26] includes the application of YOLOv4 for precise 3D microinjection, achieving notable throughput improvements and enabling large-scale genome manipulation and cryopreservation. Another study[27] employed machine learning to enhance phenotype analysis and developmental accuracy. Tools such as EmbryoNet[28] use DNN (Deep Neural Netwoks) model to identify zebrafish embryo signaling mutants in an unbiased manner whereas studies[29] and[30] have applied convolutional neural networks (CNNs) to classify phenotypes and detect abnormalities. A recent review of advanced CNN-based object detection algorithms[31] highlighted YOLO as the fastest and most effective, outperforming SSD and Faster R-CNN in speed and accuracy. This efficiency makes YOLO particularly suitable for high-throughput research of zebrafish embryos.

Despite extensive research on zebrafish embryo classification using vision-based methods, there has been limited focus on developing fast and precise sorting systems that integrate deep learning with mechanical action for embryo selection. While classification involves detecting and identifying embryos visually, sorting requires applying contact or non-contact manipulation based on those detections to separate embryos effectively. Systems such as COPAS[32] and BioSorter[33] efficiently sort large biological samples but have notable limitations, such as high costs and limited quality assessment capabilities for sorted samples. These systems rely on expensive optical components and cannot evaluate the viability or quality of sorted embryos, limiting their applicability in high-precision research. Our previous work[34] demonstrated the use of a fluidic system and robotic micromanipulator with visual servoing to sort zebrafish embryos. Compared to existing methods in the literature such as Graf et al.[22] and Breitwieser et al.[35], the system demonstrated a sorting success rate of 97.9% with a processing time of only three seconds per dead embryo, representing a significant improvement in both speed and sorting success rate.

Recent advances in microfluidics have enabled the development of sorting technologies that can automate sample processing with precise manipulation, making them well-suited for isolating individual particles or cells, as demonstrated by multiple recent studies[36–41]. These platforms require smaller sample volumes, resulting in reduced reagent costs, shorter analysis times, and less invasive sample extraction procedures for patients[37]. A key advantage of microfluidics is its closed design, which minimises the risk of cell damage and prevents contamination. Gentle sample handling and precise laminar flow control further ensure sample integrity and reduce cross-contamination. Additionally, automation and real-time monitoring further enhance safety by minimising human intervention and errors. Unlike other noncontact biological manipulation methods, such as dielectrophoresis, ultrasound, or magnetic fields, microfluidics poses no risk of damaging samples, as it does not expose them to potentially harmful external forces[42].

However, microfluidic devices have limitations, including complex and costly fabrication and maintenance processes that require specialised expertise. The small size of zebrafish embryos, approximately $1-1.3$mm in diameter, reduces the complexity of device fabrication, making microfluidics a practical and optimal choice for their handling. Hence, microfluidic devices integrated with imaging modalities can incorporate DL to analyse real-time information of zebrafish embryos and provide automated flow manipulation or resolving operational issues[23]. So, integrating microfluidic methods with DL has the potential to automate processes, potentially replacing manual manipulation steps, such as sorting and selecting zebrafish embryos, currently performed manually by researchers[43].

This study presents an original approach for zebrafish embryo sorting that combines deep learning and microfluidics. The proposed system allows millisecond detection of the stage of the zebrafish embryo and efficient sorting in a noninvasive manner. While classification systems for zebrafish embryos and robotic sorting methods are well-documented and the development of fully automated sorting systems relying solely on microfluidics remains underexplored, the technology is in its infancy, not being commercially available at the time of this writing, but has great potential for high-throughput and safe embryo handling[43]. Building on our previous work, this study proposes a novel system designed to address the limitations of earlier approaches. The reliance of the COPAS[32] and BioSorter[44] systems on costly optical components results in significant expenses and constraints on their accessibility for precise research applications. Furthermore, earlier robotic sorting methodologies presented in Diouf et al.[34] and Breitwieser et al.[35] incorporating micromanipulators are characterised by their complexity, cost, and invasive nature. The *pick-and-place* mechanisms utilising micropipettes in these systems have been observed to carry a risk of damaging embryos and potentially compromising biological integrity and viability. These limitations have thus motivated the development of a novel approach that combines microfluidics with DL to provide a reliable, precise, non-invasive, and cost-effective alternative.

The study initiated with the simulation of a CFD model to evaluate the viability of the microfluidic chip in sorting zebrafish embryos across three developmental stages (*Stage 1*, *Advanced* and *Dead*). Following simulations, the microfluidic chip is fabricated using soft lithography techniques. The study then moved to the training of a DL model via the YOLOv8 algorithm, which enables accurate embryo recognition and sorting. The design of a T-shaped separator device is then proposed, to enhance sorting efficiency by sufficiently spacing embryos in flow. The control of water flow timing within the microfluidic chip is examined, with a particular focus on the detection of a critical localization in the microfluidic channel, that will be referred in this paper as the *critical decision-making point* or *Intersection point*. The final stage of the study entailed the validation of the hypothesis that the integration of the microfluidic chip with the DL model would result in the effective sorting of embryos and the determination of the optimal parameters for the sorting system.

Results

System overview

The system consists of a microfluidic chip designed to sort zebrafish embryos, a pump system (*Kamoer Peristaltic Pump Aquarium Water Pump Flow*) controlled by a microcontroller, and a personal computer (PC) to execute a program which uses a DL model trained with *You Only Look Once version 8* (YOLOv8). The embryos are introduced into the system through channel S0 and sorted into one of three outlet channels: S3, S4, or S5, depending on their developmental stage (see Fig. 1).

The DL model is trained on a computer equipped with an *Intel Core i9–14900HX processor (32 CPUs, 2.2 GHz)*, *128 GB of RAM*, and an *NVIDIA GeForce RTX 4090 GPU*. Real-time microscopic images are used to evaluate the state of zebrafish embryos passing through channel S0. This enables the determination of whether the embryos are in the first stage of development, have died, or are in an advanced stage of development. The output of the real-time classification algorithm is employed as the input for a water flow control algorithm, which activates pumps to sort the embryos (*Stage 1*, *Dead*, or *Advanced*) into one of three outlets of the microfluidic chip, respectively S3, S4 or S5. A comprehensive illustration of the aforementioned process is depicted in Fig. 1a.

The control algorithm considers the time between image capture and embryo sorting, while mitigating disturbances. The sorting process is conducted by introducing water from channels S1 (P1) or S2 (P1) or both, and extracting it from the concerned outlet. This results in a hydrodynamic push-pull mechanism, which actuates

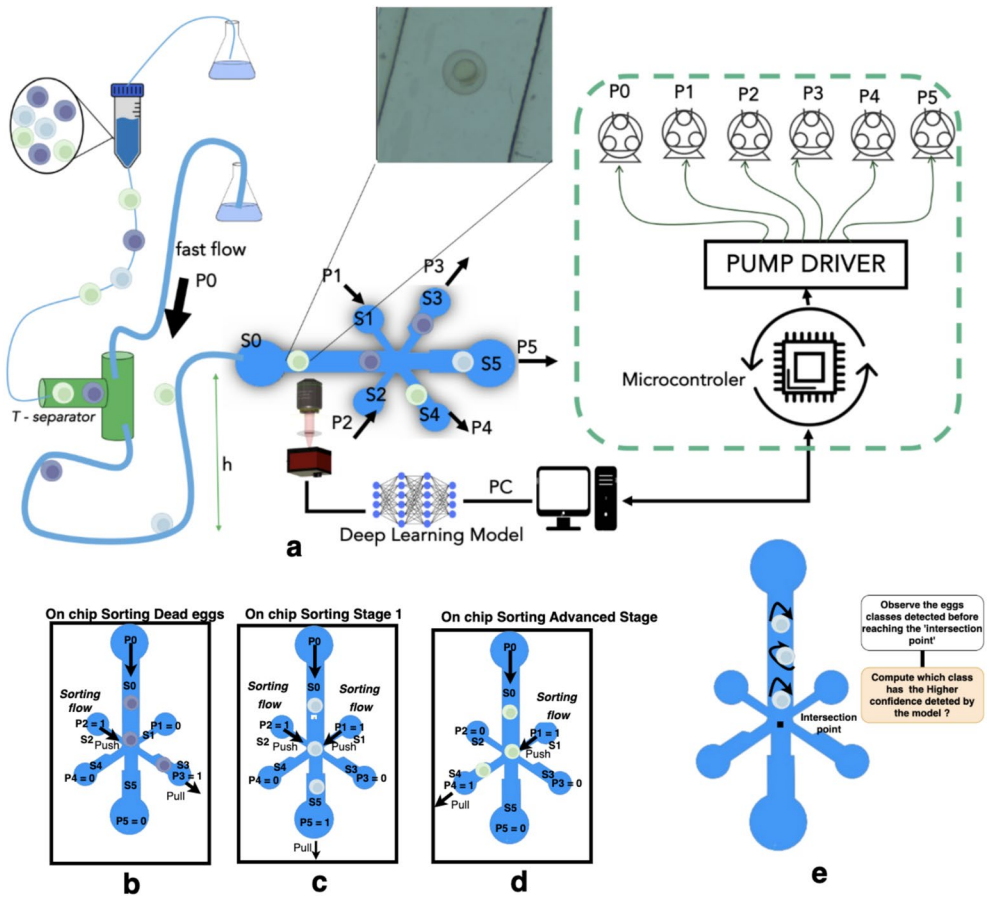

Fig. 1. Schematic overview of the sorting system. (**a**) the fluidic circuit, with input-output channels and control system. (**b**) to (**d**) fluidic sorting of detected classes. (**e**) the egg behaviour in input channel for stage detection.

the sorting process. This method minimises potential damage to cell viability and does not require specific buffer solutions[45]. The objective of pumps P3, P4 and P5 is to facilitate the extraction of the sorted embryos. The PC transmits the classification algorithm output to the microcontroller via the serial port at a data transmission speed of 115200 bauds, which is equivalent to 86.806 μs. In the event of a *Dead* embryo being identified, the P2 is triggered to redirect the lines to the outlet S3 on a provisional basis, while the P3 pump is employed to attract the embryo. In the event that a *Stage 1* embryo is present, pumps P1 and P2 are activated in unison to direct it to the centre, while pump P5 initiates a pull. Figure 1b-c-d illustrates the sorting phases. The T-shaped separator arranges embryos in the water flow, creating gaps to enable individual handling and analysis without interference. This separation enhances precision during sorting and subsequent processes. The distance between the embryos is a fundamental aspect of precise analysis, sorting, or further manipulation in biotechnology or laboratory applications. Owing to the dynamic motion of zebrafish embryos which resemble a ball in fluid, a critical decision-making point, termed the *Intersection point* is defined within the microfluidic chip. This allows a brief observation period for accurate detection and efficient sorting. The class with the highest confidence level, as determined by the model, is selected before it reaches the *Intersection point* (see Fig. 1e).

Computational Fluid Dynamics (CFD) simulation results

A CFD simulation is conducted to analyse the fluid dynamics involved in sorting zebrafish embryos within the microfluidic device. Zebrafish embryos are modelled as 1 mm spherical particles and introduced into the chip with a 2-second delay. The fixed sorting parameters used in the numerical simulation are : fluid dynamic viscosity (8.90×10^{-4} Pa.s), fluid density (997 kg/m^3), particle density (1050 kg/m^3) and particle diameter (1 mm). The simulation utilised coloured dots to represent zebrafish embryos. The model consists of two steps: a stationary step to generate the velocity profile along the channel and a time-dependent step, during which the particle path is calculated using equations presented in the Methods section, **Computational Fluid Dynamics (CFD) Modelling**. Once convergence is achieved, the results are analyzed. To determine the optimal pump flow rates for effective sorting, the flow rate of pump P0 (responsible for driving embryos into the main entry channel S0) is fixed. Two velocity configurations are then tested for sorting pumps P1 and P2. To identify good flow values for achieving satisfactory sorting of a *Dead* egg, in other words, the embryo should be redirected into the S3 channel. Tests are conducted with $v_{S0} = v_{S1}$ (**Test 1**) and then $v_{S1} = 2 \times v_{S0}$ (**Test 2**), with v_{Sx} the velocity of the flow of channel *x* in m/s. The flow rate of each pump is denoted as Q_{Sx}.

Given the symmetric design of the chip, the flow parameters from **Test 2** can be directly applied to sort particles (see Fig. 2c-d). This sorting mechanism relies on the principle of bifurcation, commonly referred to as the Zweifach-Fung effect. The following definition is proposed:

$$\alpha = \frac{Q_{Sx}}{Q_{Sy}} \tag{1}$$

where Q_{Sx} and Q_{Sy} are the flow rates of Px and Py, respectively. For example, if α is greater than 1, particles will be directed towards the Sx channel. This implies that the sorting process is contingent upon the flow rates of the desired direction being sufficiently robust to counterbalance the opposing flow. In the case of sorting on the left outlet (S4), $\alpha_1 = \frac{Q_{S4}}{Q_{S5}}$ and $\alpha_2 = \frac{Q_{S4}}{Q_{S3}}$; in order for the embryo to be correctly sorted into S3, both α_1 and α_2 must be greater than 1. Furthermore, the particles experience a torque that pulls them towards the S4 channel due to the asymmetric distribution of shear forces, where $\gamma_{S4} > \gamma_{S3}$ and $\gamma_{S4} > \gamma_{S5}$. In light of the prevailing conditions, the selection of the appropriate flow rate for the system's pumps is undertaken with a view to achieving the desired particle separation. To direct the particles in the middle, the two pumps P1 and P2 are activated simultaneously, thereby directing the flow to the middle. CFD simulation results for sorting into the right outlet and the middle outlet can be find in the **Supplementary materials, Section S2, Figure S2, S3, S4**. The CFD simulation facilitates the evaluation of the feasibility of embryo sorting within a microfluidic chip by means of analysis of fluid dynamics and flow interactions. Through the utilisation of computational modelling, insights are provided into the influence of flow rates and channel configurations on embryo trajectory, thereby facilitating the determination of sorting conditions. **Test 2** is determined to be the correct one because it introduces a controlled velocity contrast between the channels, which allows for a more effective deflection of the embryos into the desired channels. By setting $2 \times v_{S0} = v_{S1}$, this configuration creates a differential flow force that better directs the embryos, ensuring efficient sorting. The increased velocity in channels S1 and S2 enables the system to guide the embryos with greater precision, thus making it the optimal setup for sorting when compared to the equal velocities in **Test 1**. The simulation has been designed to replicate the microfluidic chip conditions, thereby ensuring that the specified channel dimensions are adhered to. By adhering to these design parameters, the simulation accurately reflects the actual fluid dynamics and sorting behaviour of the system, thus permitting the determination of the criteria for pump settings a for sorting.

Following the determination of the fluid speed conditions between channels for the sorting of embryos, the subsequent simulation aims to ascertain the distribution of fluid-induced shear stress across the microfluidic domain during the sorting process, with particular reference to embryo positioning. The analysis is of twofold purpose: firstly, to identify the region of maximum mechanical load during sorting, and secondly, to quantify whether the induced stress remains within biologically safe levels. Three representative embryo locations are selected for further analysis: at the inlet (embryo 1), in the central junction (embryo 2), and downstream in the outlet S4 (embryo 3). The wall shear stress τ_w is computed from the velocity gradient at the fluid–solid interface using:

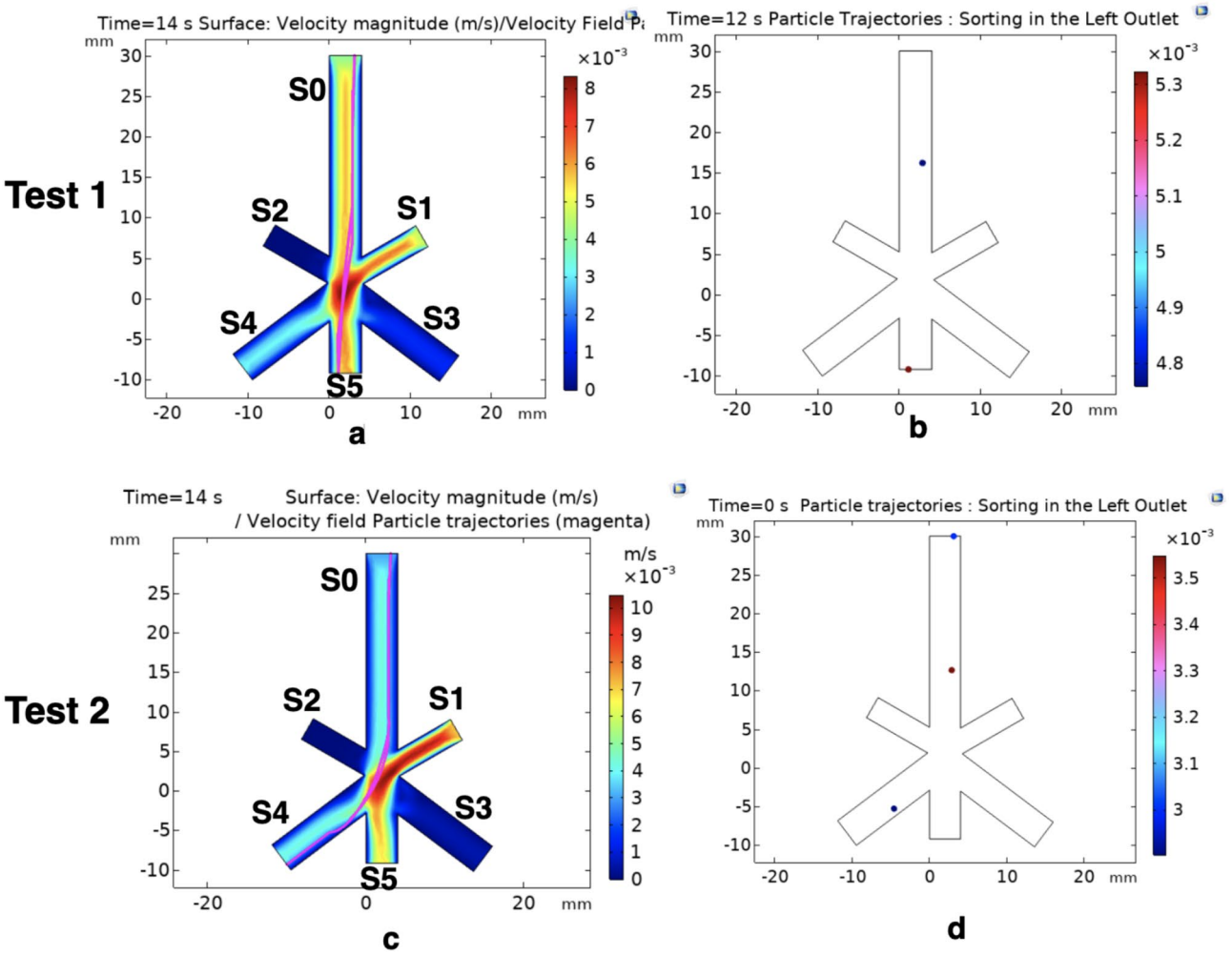

Fig. 2. **(a** and **b)** CFD simulation results for attempting sorting into the left outlet (**Test 1**) with uniform flow velocities $v_{S0} = v_{S1}$. Velocity profile with $Q_{S0} = 3000$ μl/min and $Q_{S1} = 600\,\mu$l/min corresponding to $v_{S0} = v_{S1} = 0.004$ m/s for the given chip configuration. Trajectories (in magenta) and (**b)** shows failure to push particles in the left channel due to insufficient counteracting force from the opposite side. (**c** and **d)** same simulation (**Test 2**) with $2 \times v_{S0} = v_{S1}$. Velocity profile with $Q_{S0} = 3000$ μl/min and $Q_{S1} = 1200$ μl/min corresponding to $2 \times v_{S0} = v_{S1} = 0.008$ m/s for the given chip configuration. **Test 2** yields satisfactory results, ie the magenta line and (**d)** demonstrate that the embryos are correctly sorted, driven by the force from the opposite side. The higher pressure gradient effectively guides the particles toward the desired channel.

$$\tau_w = \mu \left(\frac{\partial u_t}{\partial n} \right) \tag{2}$$

where u_t is the tangential velocity and $\partial u_t / \partial n$ is the gradient normal to the surface. Because the embryos are modeled as rigid bodies, shear stress is evaluated specifically around the surface of each embryo. To quantify the overall mechanical exposure, the total shear stress magnitude τ is also computed from its directional components using:

$$\tau = \sqrt{\tau_x^2 + \tau_y^2 + \tau_z^2} \tag{3}$$

This scalar value provides a norm of the full vectorial shear distribution experienced by the embryo in the surrounding fluid domain. As demonstrated in Fig. 3.a-b, CFD results using Equation 3 reveal the presence of localised peaks of shear stress around the embryo located at the central junction (Embryo 2), where S0 and S1 flows converge. The shear values at this point reach approximately 0.027 Pa, thus identifying this junction as the critical sorting site. It is noteworthy that the side of embryo 2 which aligned with the incoming flow from S1 appeared redder, indicating an asymmetric stress distribution consistent with directional shear impact.

Figure 3c quantifies the maximum shear stress applied to zebrafish embryos positioned at three critical regions (inlet, junction, and outlet) under increasing flow velocities (v_{S0}, with $v_{S1} = 2 \times v_{S0}$). The objective of this study is to ascertain the safe operational range of flow speeds that ensure shear exposure remains below

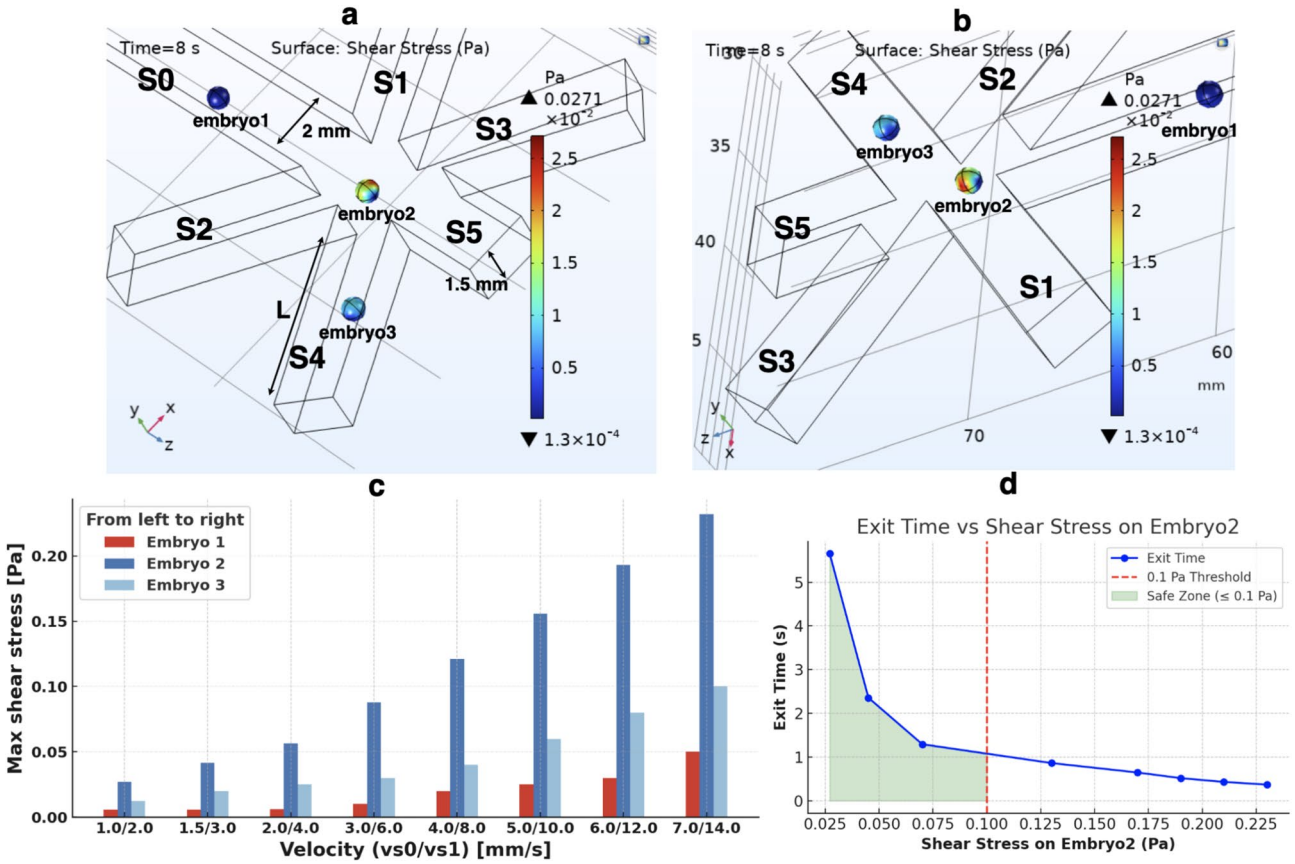

Fig. 3. (**a, b**) CFD simulations of wall shear stress (Pa) at t = 8 s in the microfluidic chip used to sort zebrafish embryos. (**b**) is an opposite view of (**a**). Three embryos are positioned in distinct branches (Embryo 1 in S0, embryo 2 in the junction, and Embryo 3 in the outlet S4). The color scale highlights the magnitude of surface shear stress, showing stress accumulation primarily at the junction (Embryo 2), where sorting occurs. The lateral deflection flow is introduced from channel S1, oriented at 45° relative to the outlet channel. The simulation corresponds to flow conditions of v_{S0}= 0.001 m/s and v_{S1}= 0.002 m/s. The embryo is modeled as a rigid sphere inclusion located at key positions along the sorting path. No-slip boundary conditions are applied, and flow is considered steady-state and laminar. **c** Maximum shear stress measured at the three embryonic positions for increasing flow conditions, defined as pairs (v_{S0}/v_{S1}) in mm/s. Embryo 2, located at the central junction, consistently exhibits the highest shear exposure. Embryo 3, downstream in S4, experiences intermediate levels, while embryo 1 (initial position) is exposed to the lowest stress. (**d**) Correlation between shear stress at the junction (embryo 2) and embryo exit time through outlet S4, modeled using a two-phase transport equation accounting for geometry-based velocity projection. A nonlinear inverse relationship is observed, with a saturation effect at high shear levels. The green shaded area denotes the safety zone ($\leq 0.1Pa$), above which shear stress may compromise embryo viability. The red dashed line indicates the biological threshold.

acceptable levels for zebrafish embryos. Shear stress is extracted from the embryo surface using CFD simulations for velocities ranging from 1 to 7 mm/s. Please refer to the table **Supplementary Table S1**, for a comprehensive overview of the results.

The findings of this study corroborate the efficacy of the design in localising mechanical load during the sorting process, while concurrently ensuring mechanical safety in other regions. Akagi et al.[46] have demonstrated that shear stress levels of less than 0.1 Pa do not appear to be associated with deleterious effects on zebrafish embryonic development. However, values above this threshold may potentially compromise viability or morphogenesis. Considering the configuration and dimensions of the microfluidic chip, as well as the threshold value, safe sorting can be achieved for v_{S0} values below 4 mm/s.

This first study investigated the relationship between local shear stress and sorting dynamics in a microfluidic device designed for zebrafish embryo handling. The next study specifically examines how increasing shear stress applied at the sorting junction where embryo 2 is located affects the downstream transit time of the embryo through the outlet channel (S4). The analysis is predicated on the stress quantification performed in Fig. 3d, employing the same shear stress values extracted from surface measurements around embryo 2 under varying actuation flow rates. The transport model utilised in this study incorporates the actual chip geometry, wherein the base flow (v_{S0}) enters the junction at 45°, while the sorting pulse (v_{S1}) is aligned with the outlet channel. During the 1.5-second actuation period, the embryo is subjected to both flows, with each contributing differently

to the forward motion depending on their alignment. Subsequent to this phase, the sole remaining component of the embryo that continues to move is the axial base. The combined effect is such that the resultant transport regime is comprised of two phases. The solution to this problem yields the following expression for the total exit time:

$$t_{\text{exit}} = \begin{cases} \dfrac{L}{V_{S1} + \cos(45°) \cdot V_{S0}}, & \text{if } d_1 \geq L \\ 1.5 + \dfrac{L - d_1}{\cos(45°) \cdot V_{S0}}, & \text{otherwise} \end{cases} \quad \text{with } d_1 = 1.5 \cdot (V_{S1} + \cos(45°) \cdot V_{S0} \tag{4}$$

with L, the lenght of the channel S4 (See Fig. 3a). Full derivation, modeling details are provided in the **Supplementary material, Section S4**. Using exit times calculated with Equation 4, Fig. 3d illustrates a non-linear inverse relationship between shear stress at the sorting junction and the embryo's clearance time from the outlet. Please refer to **Supplementary Table S2** for a comprehensive overview of the results presented in Fig. 3d. As the magnitude of shear stress increases, the rate of sorting becomes significantly faster, indicating that enhanced hydrodynamic forcing effectively propels the embryo downstream. However, this acceleration exhibits diminishing returns beyond approximately 0.15 Pa, suggesting that the system approaches a performance plateau where further increases in flow intensity no longer yield proportionate reductions in exit time. This behaviour is indicative of a fundamental trade-off in the microfluidic sorting design. It is evident that an augmentation in flow rates engenders a concomitant improvement in throughput and sorting responsiveness. Conversely, excessive mechanical stress has the potential to compromise the physical integrity or developmental potential of the embryo. This is of particular significance for fragile specimens, such as zebrafish embryos, which exhibit limited tolerance to shear. The existence of a saturation zone is indicative of the presence of an optimal range of flow parameters, which are mechanically sufficient to ensure sorting yet biologically safe.

These findings enable the precise quantification of embryo exposure under varying flow conditions and informed the development of a transport model linking stress to sorting time. This facilitates the delineation of a safe operating window (≤ 0.1 Pa) and informed design decisions pertaining to geometry and flow rate. The simulations furnished a robust framework for the enhancement of sorting performance, whilst ensuring the preservation of embryo viability.

Model training results for zebrafish embryo detection

During the first model training, the network is trained for 100 epochs with a momentum of 0.932. The initial learning rate is set to 0.01 and gradually decreases to a final value of 0.0001, with a weight decay of 0.0005 to prevent overfitting. A batch size of 8 is used, and input images are resized to 640×640 pixels. The optimization is performed using Stochastic Gradient Descent (SGD), and a Mosaic data augmentation strategy is applied to enhance the model's generalization capabilities. The dataset is initially trained with a default model of YOLOv8m (medium). The hyperparameters of YOLOv8 are subsequently optimized by employing a genetic algorithm aimed at maximising the fitness score over 300 generations. Figure 4**c** illustrates the evolution of the fitness score across generations. Generation 127 offers a superior fitness score and is selected for further study. A comparison of the initial and tuned YOLOv8 hyperparameters can be found in the **Supplementary Table S4 in Section S5**.

Table 1 provides a global and comprehensive comparison between the default and optimised models. The weighting of the fitness score has been designed to prioritise accurate spatial localisation and generalisation across object scales. However, class-level precision and recall have been deliberately excluded from the fitness function. This approach is indicative of a focus on the quality of detection, particularly in scenarios where the capacity to delineate tight bounding boxes and the demonstration of robust performance across variable embryo morphology are deemed to be of greater significance than the attainment of raw classification counts. Across all embryo types, the Optimised model enhances *mAP@0.5* from 0.964 to 0.976 (+1.2 %) and *mAP@0.5:0.95* from 0.872 to 0.886 (+1.6 %). Although the performance improvements between the two models remain relatively modest (ranging from 1 % to 2 %), they may still be meaningful in the context of object detection, especially when the baseline model is already performing at a high level. These enhancements suggest an augmented capacity to localise and classify embryos with greater precision, particularly under more stringent IoU constraints. However, precision and recall both decrease slightly (– 0.9 % and – 0.8 %, respectively), indicating a trade-off: the model becomes more sensitive to complex or low-confidence cases, resulting in more false positives and a minor increase in false negatives. *Stage 1* embryos, representing early developmental phases, are visually simple with limited contrast.

The Optimised model enhances both precision (+2.6 %) and recall (+1.3 %) in comparison to the default model. However, *mAP@0.5:0.95* demonstrates only a marginal increase (+0.6%). This finding suggests that, while the detection process demonstrates increased consistency, precise bounding box localization remains challenging, a phenomenon that is probably attributable to the transparency and uniform structure of the embryos. *Advanced* embryos, which present complex morphology including somites and developing organs, benefit from a strong recall improvement (+6.1 %) and a +2.0 % gain in *mAP@0.5:0.95*. The decline in precision by 1.9 % suggests potential over-detection in denser or visually complex scenes. However, the enhancement in overall performance is indicative of an improved handling of inter-individual variability. The presence of dark pigmentation, high contrast, or morphological disintegration in *Dead* embryos often leads to ambiguity, distinguishing them from other samples. The Optimised model has been shown to achieve a +1.8 % increase in recall and the highest *mAP@0.5:0.95* improvement across all classes (+2.3 %), indicating an enhancement in sensitivity to degraded structures. Conversely, precision undergoes a decline from 0.925 to 0.894, indicating an increase in false positives. This decline in precision could be attributed to misclassification of dark background regions or the presence of imaging artefacts that resemble dead embryos. The advantage of the optimised model

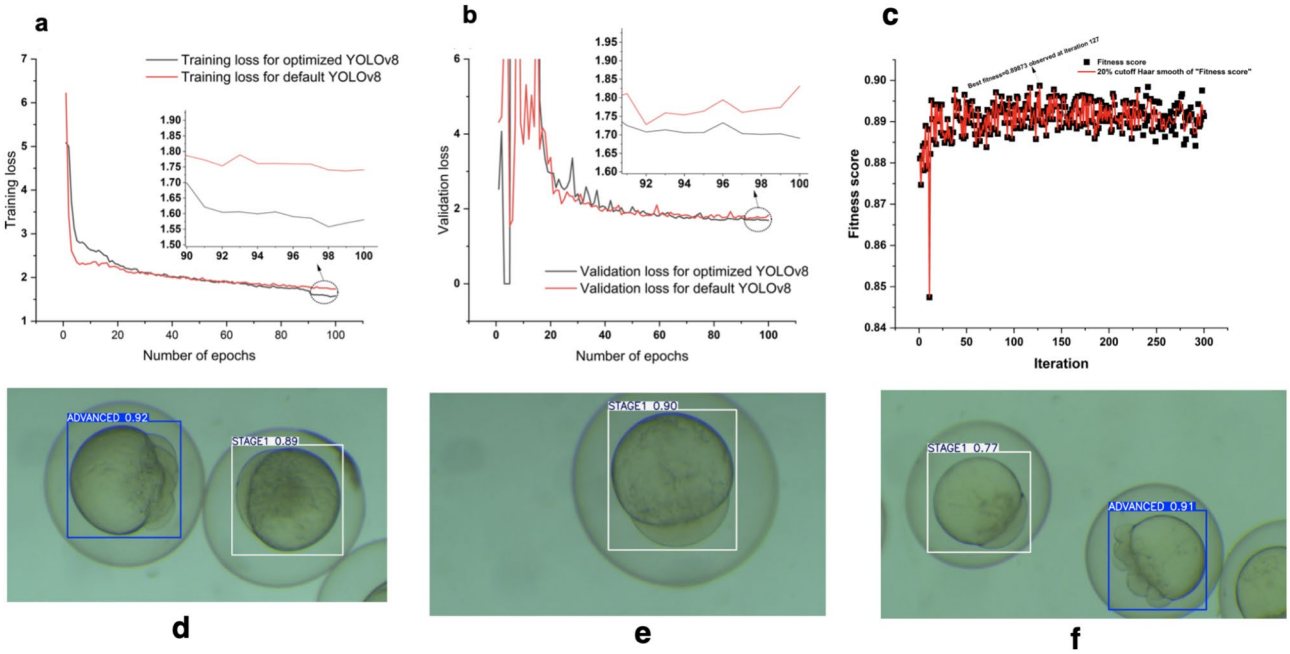

Fig. 4. Comparison of training dynamics, fitness optimization, and qualitative predictions between Default and Optimised YOLOv8 models. (**a)** Training loss curves for Default (red) and Optimised (black) models over 100 epochs. The Optimised model converges faster and stabilizes at a lower loss value, indicating improved learning efficiency. (**b)** Validation loss curves show that the Optimised model generalizes better to unseen data, with consistently lower validation loss, particularly in later epochs (inset). (**c**) Evolution of the fitness score across 300 hyperparameter tuning iterations. The best configuration is identified at iteration 127 with a fitness score of 0.8927, based on a weighted function emphasizing mAP@0.5:0.95. A smoothed curve using 20% cutoff Haar transform is overlaid. (**d**-**f)** Sample inference results on zebrafish embryos showing successful detection and classification into stages (e.g., *Stage1* and *Advanced*) with associated confidence scores, illustrating the practical performance of the optimized YOLOv8 in real microscopic images.

Class/Metric	Images	Instances	P (D)	P (O)	R (D)	R (O)	mAP@0.5 (D)	mAP@0.5 (O)	mAP@0.5:0.95 (D)	mAP@0.5:0.95 (O)
ALL	134	273	0.919	0.91	0.964	0.956	0.964	0.976	0.872	0.886
Advanced	134	109	0.933	0.914	0.899	0.954	0.958	0.966	0.859	0.876
Dead	134	52	0.925	0.894	0.955	0.972	0.969	0.989	0.879	0.899
Stage 1	134	112	0.898	0.921	0.929	0.941	0.963	0.973	0.878	0.884

Table 1. Comparison of YOLOv8 models on the test set, where D stands for Default and O stands for Optimised. The evaluation is conducted across four categories : ALL, *Advanced*, *Dead*, and *Stage 1*, using standard object detection metrics presented in **Methods** section **Description and evaluation of YOLOv8 algorithm**: Precision (P), Recall (R), and mean Average Precision (*mAP*) at IoU thresholds of 0.5 and a range from 0.5 to 0.95.

is also evidenced by the loss curves of the models (see Fig. 4a-b). The training loss is a measure used to evaluate how well a deep learning model aligns with the training data. It reflects the model's error on the training set and indicates how well the model fits the dataset. It is expected to decrease over time as the model learns from the dataset, which is the case in this study (see Fig. 4a). However, a very low training loss does not necessarily guarantee good performance on new, unseen data, as the model may have overfit the training data. Therefore, the validation loss is useful in assessing the model's ability to generalise to unseen data during training (see Fig. 4b). For both models (default and optimised), the loss curves exhibited a decreasing trend, but it is evident that the loss curves of the optimised model converge closer toward zero. This indicates that the optimised model benefits from improved hyperparameter settings (e.g., learning rate schedule, batch size, or data augmentation...) that enhance gradient stability and convergence speed. The smoother descent and lower final training loss suggest more efficient parameter updates and better fitting of the training distribution, without signs of early stagnation.

Both models achieved high accuracies, demonstrating successful training. However, the optimised model is selected exactly at the 127th generation for further experimentation due to its superior performance (see Fig. 4c). The reduced validation loss of the optimised model implies better generalisation to unseen data. It suggests that the chosen hyperparameters enhance the model's ability to extract robust features while avoiding

overfitting. Lower variance in the validation curve also reflects improved regularization and higher resilience to noise or dataset imbalance.

With the same GPU used for training, the optimized YOLOv8 model was evaluated using a separate testing dataset consisting of 273 annotated images of zebrafish embryos, which were not part of the training phase. The model achieved an accuracy of 100 % in correctly detecting and localizing all zebrafish embryos in the test set, with high confidence scores for each detection, indicating both precision and reliability. Furthermore, the model demonstrated real-time performance, with an average inference speed of 10.5 ms per image when executed on the same GPU used for training. The Fig. 4d-f depict examples of the detection of zebrafish embryos from the testing dataset.

T-shaped separator device

After successfully training the model and achieving satisfactory results, the next step is to optimise the method for embryos in the chip to ensure accurate sorting. Since embryos leave input the reservoir in a random manner, there are instances where two embryos may be positioned too close together. This poses a challenge because the system relies on sequential detection by the DL model, followed by fluid deviation and sorting. If two embryos simultaneously enter the field of view of the camera, as depicted in Fig. 5a, it could disrupt the sorting process. Therefore, a robust embryo separation mechanism is called for maintaining sorting accuracy. The process ensures that embryos are spaced at a minimum distance d, as shown in Fig. 5b, to prevent complications arising from fluid dynamics and to guarantee smooth operation.

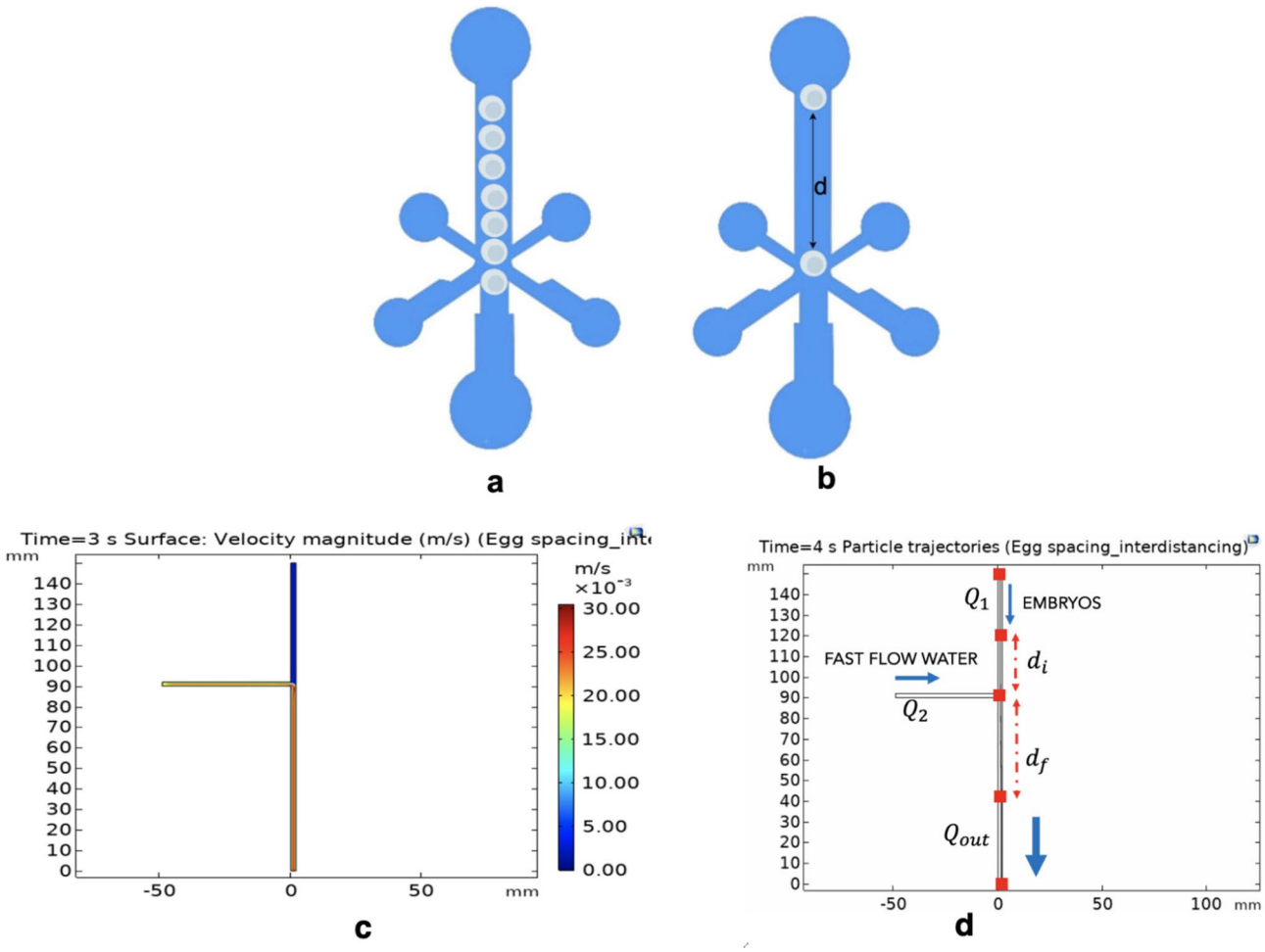

Fig. 5. Visual representation of embryo spacing dynamics during the sorting process with gravity-assisted flow. (**a**) Example of poor embryo separation, where embryos are too closely spaced, leading to potential sorting errors. (**b**) Schematic illustrating proper embryo separation with a defined minimum distance d between embryos to ensure accurate sorting. (**c**) CFD simulation of velocity magnitude in a T-shaped microfluidic separator at 3 s. Gravity is applied to direct the fluid flow downward, guiding all fluid and embryos into a unified trajectory. (**d**) Simulated particle trajectories (red dots representing embryos). The primary inlet flow rate Q_1 propels the embryos along the central axis, while the lateral flow rate Q_2 acts perpendicularly to adjust inter-embryo spacing. Gravity complements these forces by enhancing directional control of the main stream toward the outlet Q_{out}. Embryo spacing increases from initial distance d_i to final distance d_f, facilitating reliable downstream processing.

The present study draws inspiration from the principles of a variable-speed conveyor system for the purpose of achieving embryo separation. By adjusting the speed at which the embryos are transported, the system effectively facilitates their separation. The design incorporates a T-shaped separator that directs two distinct flows. One branch of the T channels carries a flow containing embryos entering the separator, while the other branch carries a fast-moving fluid devoid of embryos. Both flows converge at a single outlet, where the fast-moving fluid generates a separation effect between the embryos as they pass through the T-shaped separator.

In order to evaluate the feasibility of this approach, a computational fluid dynamics (CFD) simulation is conducted. The simulation used a modeling approach similar to that used for sorting within the chip, with the key difference being the use of gravity to ensure a uniform and direct fluid outlet at the T-shaped separator. The simulation is based on Newton's second law and the governing equation for particle tracing, as expressed in Equations 5 and 6.

$$m_p.\frac{dv_p}{dt} = F_D + F_g \tag{5}$$

Where F_D is the drag force, v_p is particle velocity, m_p is particle mass, F_D and F_g are the drag and gravity. So, the governing equation for particle tracing is expressed as follows:

$$\begin{aligned} F_D + F_g &= \frac{1}{\tau_p}.m_p(U - v_p) \qquad \text{with } \tau_p = \frac{4\rho_p d_p^2}{3\mu C_D R_{e_r}}, \\ C_D &= \frac{24}{R_{e_r}}(1 + 0.15R_{e_r}^{0.687}) \qquad , \\ R_{e_r} &= \frac{\rho|U - v_p|d_p}{\mu} \end{aligned} \tag{6}$$

where F_D is the drag force, F_g is the gravity force, v_p is particle velocity, m_p is particle mass, ρ_p is particle density, and d_p is particle diameter, R_{e_r} the relative Reynolds number, ρ density of the fluid and μ dynamic viscosity of the fluid. The simulation results are presented in Fig. 5c-d.

This simulation demonstrates the impact of the lateral water flow (Q_2) on the spacing and trajectory of the embryos as they pass through the separator. The embryo spacing appears to increase from d_i to d_f, indicating the potential influence of the lateral flow. In order to model the distance between embryos in the T-shaped separator setup, an equation is defined which relates the initial distance d_i between embryos to their final distance, d_f. This equation takes into account the influence of the flows, Q_1 and Q_2. The velocity of the lateral flow, denoted by Q_2, exerts an influence on the embryos, resulting in an increase in their separation depending on the relative velocity of the two flows. The distance between the embryos as a function of time can be expressed by the following equation:

$$d_f = d_i + v_{\text{rel}} \cdot t \tag{7}$$

where d_f is the final distance between the embryos after being influenced by the lateral flow, d_i is the initial distance between the embryos when they first enter the section influenced by Q_2, v_{rel} is the relative velocity between the lateral flow Q_2 and the main flow Q_1 and t is the time during which the embryos are affected by the lateral flow Q_2. Given the specified flow rates, Q_1 and Q_2, the velocities can be expressed in terms of these flow rates. The velocity, designated as v, in each branch is given by: $v = \frac{Q}{A}$ where Q is the flow rate and A is the cross-sectional area of the branch. Given that the same pipe is employed for all setup, $A_1 = A_2 = A$, so $v_{Q_1} = \frac{Q_1}{A}$ and $v_{Q_2} = \frac{Q_2}{A}$. The relative velocity v_{rel} between the two flows (main flow and lateral flow) becomes: $v_{\text{rel}} = v_{Q_2} - v_{Q_1} = \frac{Q_2}{A} - \frac{Q_1}{A} = \frac{Q_2 - Q_1}{A}$. Substituting v_{rel} into the equation 7 for d_f, it is obtained :

$$d_f = d_i + \frac{(Q_2 - Q_1) \cdot t}{A} \tag{8}$$

where t denotes the time during which the embryos are exposed to the influence of the lateral flow Q_2. The modelling of the T-shaped separator provides the flexibility to act on the components in order to achieve the desired distance of separation. Equation 8 indicates that the final distance d_f between the embryos depends on four parameters: the initial distance between two embryos entering in the T, the larger the difference between Q_2 and Q_1, the greater is the impact on the embryo spacing. The cross-sectional area A affects the relative velocity between the two flows. In this case, since A is the same for both branches, it simplifies the relationship between the velocities. Finally, the longer the embryos are exposed to the lateral flow Q_2, the greater the change in their spacing.

This model allows the calculation of the expected increase in distance $d_f - d_i$ between the embryos based on the flow conditions. By employing specific values for Q_1, Q_2, A, and t, one can insert them into this equation to ascertain the final spacing d_f between the embryos. The general expression of d_f is :

$$d_f = d_i + (\frac{Q_2}{A_2} - \frac{Q_1}{A_1}) \cdot t \tag{9}$$

In this study the same dimension is utilised for the T branches, however, further refinements are necessary to optimise the separator's geometry. For instance, narrowing the lateral flow channel (reducing A_2) could increase the acceleration and improve separation (see Equation 9). Additionally, extending the exposure time (length

of the pipe) or employing pulsatile flow could ensure more consistent spacing under varying experimental conditions.

Control Mechanism for waterflow timing at microfluidic junctions

To ensure optimal and continuous sorting in a rapid system, a critical decision point must be established where the timing of waterflow is controlled to direct embryos into the appropriate outlet channel. Embryos, which can be conceptualized as floating spheres in water, are capable of changing position and orientation as they move through the system. Consequently, an embryo entering the field of view may be detected multiple times in different orientations. The principal algorithm determines the most confident classification on the basis of these detections. The central decision point, referred to as the *Intersection point* marks the location where the sorting decision is finalised, and the process of redirecting the embryo to its designated outlet channel begins. To achieve this, a simple comparison is made between the pixel coordinates of the embryo's detected center and the coordinates of the *Intersection point* prior to initiating the deviation process to the correct channel. A methodology is developed to identify this *Intersection point* regardless of the microfluidic chip's position or orientation. It is defined as the point of intersection of the midlines of the three inlet channels (S0, S1, S2). *ImageJ*, an image analysis software, is utilized to mark and analyze specific points within the microfluidic chip using thin black lines (see Fig. 6X.a). The *Intersection point* is highlighted with the pixel coordinates $x = 1086$, $y = 877$ and displayed in a magnified view in Fig. 6X.a. Utilising the methodology developed during this study, the coordinates of the *Intersection point* are found to be slightly different, namely $x = 1085$, $y = 869$ and are marked in blue in Fig. 6X.b. In order to achieve the results depicted in Fig. 6X.b, a series of procedures is followed. A separate YOLOv8 model is first trained to detect the edges of the microfluidic chip labelled as *wall*. A total of 500 images of the microfluidic chip are captured via the same microscope that are employed for training the zebrafish embryo classification model. The *Roboflow* tool is employed to label the edges of the microfluidic chip

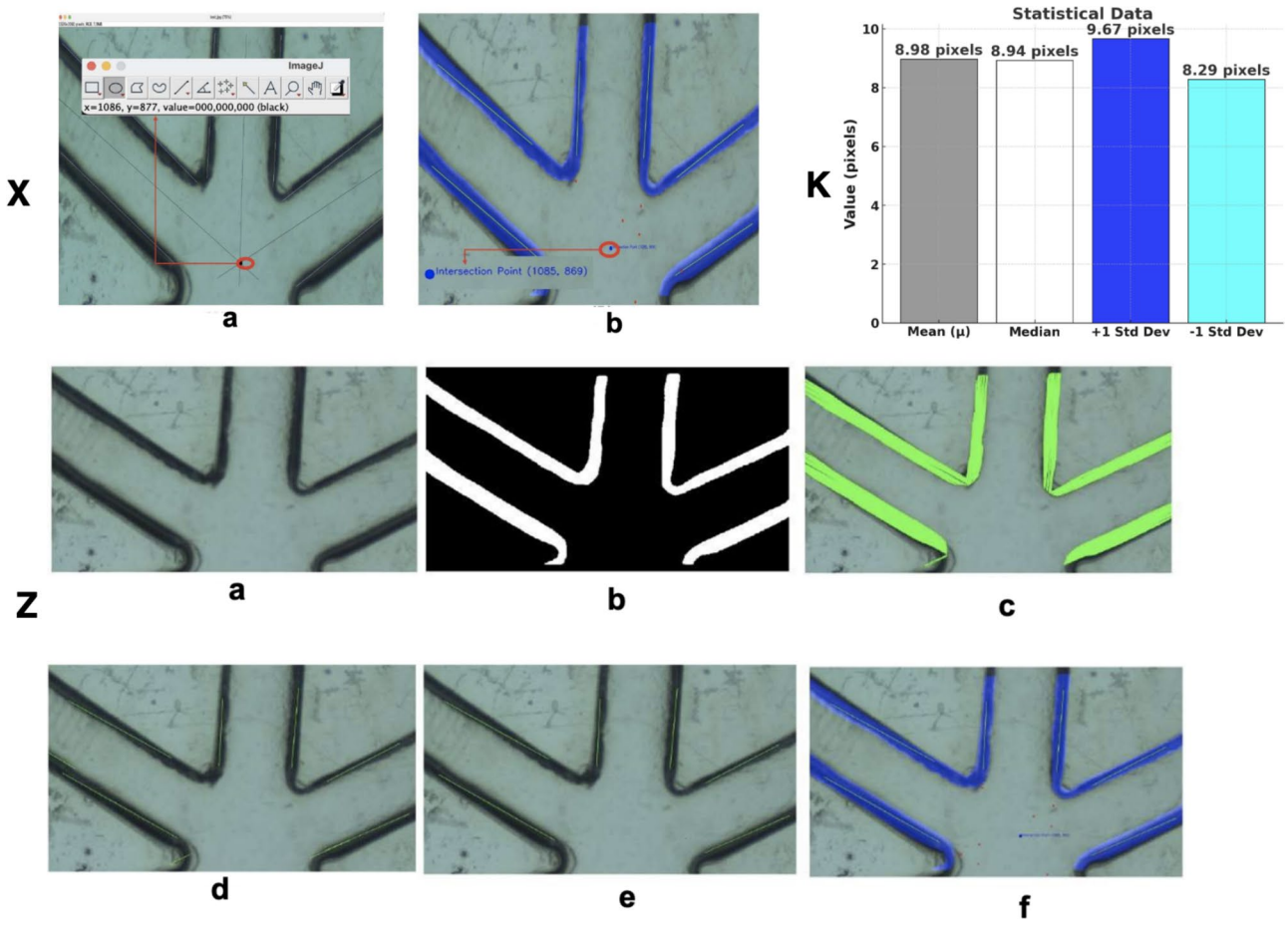

Fig. 6. Detection and analysis of intersection points within a microfluidic chip using image processing techniques. **X**: Identification of *Intersection point* pixel coordinates using (**a**) *ImageJ* and (**b**) the developed method. **Z**: Step-by-step illustration of the feature detection process to achieve the result of image **X.b** : **a**. original image frame, (**b**) edge detection and segmentation, (**c**) line detection using the Hough transform, (**d**) averaged lines and clustering via the DBSCAN algorithm, (**e**) filtered lines, and (**f**) final computed intersection lines and centroid intersection point. **K**: Statistical metrics representing the errors, including mean, median, and standard deviations, quantifying the robustness, accuracy, and consistency of intersection point detection using a test set of 61 images.

(see Supplementary material). The YOLOv8s-seg (YOLOv8 Instance Segmentation small model) is employed for model training for 100 epochs. Table 2 demonstrates satisfactory training results, **see Supplementary material Section S5 : Deep learning model for segmenting the edges of the microfluidic chip and Supplementary Figure S8** for more details about this training.

```
Initialize: Load YOLO model and set device to CUDA if available
procedure MAIN(image_path)
    Read the frame
    if frame is None then
        Print Error message and return
    end if
    Detect edges: Run YOLOv8 segmentation model on the frame and create an edge map
    Detect lines: Use Hough Transform on the edge map to detect lines
    if lines are detected then
        Cluster lines: Group detected lines by angle and distance using DBSCAN algorithm
        Average lines: Compute average lines for each cluster
        Filter lines: Filter average lines by length
        Compute intersections: Find intersection points of filtered lines
        Center of mass: Calculate center of mass of intersections
        Visualize: Display the lines and Intersection points on the frame
    else
        Print "No lines detected"
    end if
end procedure
Call Main(frame)
```

Algorithm 1. Detection and Visualization of *Intersection point*

The Algorithm (1) is designed for detecting the *Intersection point* employing a combination of DL and traditional computer vision techniques. Figure 6Z.a to Fig. 6Z.f depict all the process. It commences with the loading of a YOLOv8 model, which is employed to generate an edge map of the inlet frame. The Hough transform is subsequently applied to detect lines within the aforementioned edge map. In the event of the detection of lines, the algorithm clusters them based on their angle and distance, utilising the Density-based Spatial Clustering of Applications with Noise (DBSCAN) algorithm. DBSCAN is used to cluster lines on the basis of proximity and orientation, which helps in identifying groups of parallel or similarly oriented lines. Thereafter, an average line is calculated for each cluster and lines are filtered by length to focus on prominent structures. Subsequently, the intersection points of the filtered lines are calculated, and their centre of mass is determined to serve as the *Intersection point*.

The DL model for segmenting the edges of the microfluidic chip is tested on a dataset comprising 61 images when utilising the same GPU for training. The results demonstrated 100 % accuracy with high confidence. To provide an overall evaluation of the developed algorithm, the pixel coordinates (P_{ImageJ}) determined manually through the *ImageJ* approach for each of the 61 images in the testing dataset are compared to the corresponding image with those $(P_{Algorithm})$ obtained through the algorithm developed in this study. In order to present and analyse the results, a series of equations and statistical methods are employed. The *Error* in this analysis is calculated as the Euclidean distance between the *Intersection points* identified by *ImageJ* and the algorithm. This *Error* captures the spatial difference between the two points in a 2D plane, using relative distances $(x, y)_{\text{ImageJ}} - (x, y)_{\text{Algorithm}}$.

The graph in Fig. 6K presents a statistical evaluation of the intersection point detection method, highlighting its accuracy and reliability using the mean, median and standard deviation of *Error*. The mean error (8.98 pixels) is almost indistinguishable from the median (8.94 pixels), suggesting a symmetrical and unbiased distribution of detection errors. The proximity of these values to each other is indicative of consistent performance, devoid of any systematic deviation. The standard deviation range, spanning from 8.29 to 9.67 pixels, demonstrates a narrow spread of approximately ± 0.69 pixels around the mean, thereby indicating low variability. This narrow error margin thus confirms the precision of the method, a prerequisite for the pixel-level accuracy required in microfluidic applications. So, the data substantiate the method's robust performance with regard to consistency. However, despite the encouraging outcomes, it is important to note the presence of certain limitations. Firstly, although the variability is low, an average error of approximately 9 pixels can be significant depending on the scale of the microfluidic system under study, where each pixel can represent several microns. This has the potential to restrict the applicability of the method in scenarios necessitating sub-pixel accuracy or in contexts involving particularly intricate geometries. Secondly, the method is dependent on a number of sensitive steps, including edge detection, the Hough transform, and the DBSCAN clustering algorithm. The performance of each of these steps is contingent on parameters (thresholds, tolerances, point density) that can exert a substantial

Model	Class	Precision	Recall	mAP@0.5	mAP@0.5:0.95
YOLOv8s-seg	*wall*	0.994	0.99	0.995	0.995

Table 2. Model training results for detection of the wall of the microfluidic chip.

influence on the final result. Any variation in image quality or contrast has the potential to compromise the robustness of the algorithm. For instance, poorly defined edges or image noise could disrupt line detection or generate false positives during the clustering process. Finally, the method does not appear to dynamically correct errors or adapt to cases where the intersection is partially visible or distorted, which limits its generalisation to various experimental conditions. In conclusion, while the overall performance is satisfactory in this instance, the method exhibits limitations with regard to absolute accuracy, dependence on analysis parameters, and sensitivity to image variations. This calls for caution before any extensive implementation.

Zebrafish embryo microfluidics sorting experiment

The optimised trained DL model is employed for the sorting of zebrafish embryos experiments. The zebrafish embryos utilised in the experiments are obtained under the same conditions as those used to create the image dataset. *Dead* embryos are separated into a separate reservoir and mixed with fresh embryos in a reservoir for use during the experiments. The experiments are conducted over a period of 20 days, with approximately thirty embryos tested each day. Before starting each experiment, a comprehensive list is compiled that included the embryos located within the reservoir and their respective classifications. During the course of the experiment, meticulous records are maintained, with particular attention devoted to the potential evolution of the embryos. Fig. 7a shows the complete experimental setup and the core components of the system. The embryos are initially placed in a Falcon reservoir with a density greater than that of the surrounding medium, causing them to settle at the bottom of the reservoir. To address this issue, a pipe system has been implemented to generate bubbles beneath the medium, lifting and dispersing embryos uniformly (see Fig. 7d). As shown in Fig. 7c-d a pipe is placed at the reservoir outlet to guide the embryos into a single-file stream, driven by gravity, as they enter the microfluidic chip. Figure 7c depicts the connection between the T-shaped separator, designed and printed in resin for sorting experiments and the microfluidic chip. Since peristaltic pumps are unable to accommodate the passage of embryos safely, a filtration system (see Fig. 7e) is developed to prevent possible damage to embryos. In the setup, a mixture of water and embryos is introduced into the filter. This filter is specifically designed to allow water to flow through while retaining embryos based on their size, ensuring effective separation. After filtration, the water exits through an outlet, while the embryos remain trapped in the upper section of the system. This configuration ensures that embryos are retained for sorting without being damaged, while the filtered water is safely removed.

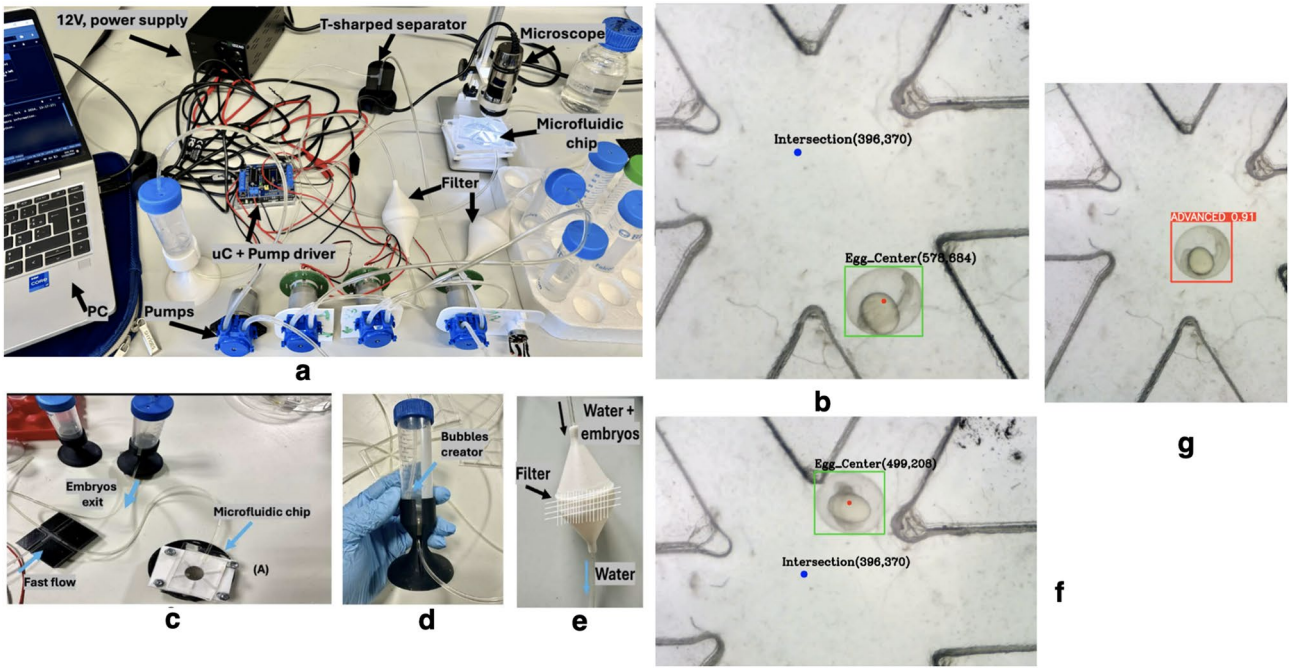

Fig. 7. Experimental setup for zebrafish embryo sorting using a microfluidic system. (**a**) Overview of the complete setup, including the microfluidic chip, microscope, microcontroller with pump driver, peristaltic pumps, power supply, and T-shaped separator. (**c**) Closer view of the microfluidic chip indicating the embryo exit path and fast flow direction. (**d**) Bubble generator used for flow manipulation within the system. (**e**) Embryo hosting and filtering unit, where water and embryos are separated by a mesh filter. (**b**) A real-time program application window that displays two functions: intersection point detection and moving embryo detection. The former involves the segmentation process, which yields the egg centre pixel coordinates. This in turn allows spatial reference analysis. (**f**) The embryo in question is being sorted in the *Advanced* Embryo part channel. (**g**) Another window that displays classification result for the same embryo identified as *Advanced* with a confidence score of 91 %. This system enables real-time detection, classification, and spatial tracking of embryos using integrated flow control and microscopy.

In Fig. 7g, the detection occurs while the zebrafish embryo is passing through the chip, demonstrating the system's ability to perform accurate classification under dynamic conditions. As illustrated in Fig. 7b and f, the *Intersection point* acts as a spatial trigger zone. Once the embryo approaches within a defined threshold distance, a decision is activated to reroute the embryo via the appropriate outlet channel based on the stored classification result. It is particularly suited for biological systems with rotational motion and unpredictable orientation dynamics, providing both accuracy and reliability in real-time microfluidic sorting. To further illustrate the performance of our approach, **Supplementary material, Movie S1** presents examples of *Advanced* embryos that are successfully detected by the deep learning model and subsequently sorted within the microfluidic chip. **Supplementary material, Movie S2** shows representative cases where the system is able to distinguish between *Advanced* and *Dead* embryos. **Supplementary material, Movie S3** illustrates cases where the system detects *Dead* embryos and subsequently sorts them within the microfluidic chip. To evaluate the efficiency of the system under test, several metrics are defined.

- **Correctly Predicted Embryos** metric represents the total number of embryos that are accurately predicted by the model as belonging to their respective classes (*Stage 1*, *Advanced*, *Dead*). It reflects the model's capacity to accurately identify embryos based on their developmental status.
- **Incorrectly Predicted Embryos** metric enumerates the number of embryos that are misclassified by the model, indicating that they are predicted to belong to a different class than they actually do. A lower number is indicative of enhanced predictive accuracy and model performance.
- **Correctly Sorted Embryos** metric indicates the number of embryos that are not only correctly predicted but also accurately sorted. This metric reflects the efficacy of the sorting process in categorising embryos based on the predictions made.
- **Incorrectly Sorted Embryos** metric quantifies the number of embryos that are both incorrectly predicted and misclassified during the sorting process. It reflects the inefficiencies in sorting, which can impact downstream applications and analyses.
- **Total Number of Embryos** metric denotes the total count of embryos evaluated in each class.
- **Accuracy** representes the ratio of correctly predicted embryos to the total number of embryos. A higher accuracy value indicates a more reliable predictive model, as it demonstrates a greater capacity to accurately predict the outcome.
- **Sorting Efficiency** assesses the efficacy of the system in sorting the predicted embryos. It is calculated as the ratio of correctly sorted embryos to the total number of embryos, expressed as a percentage. A high sorting efficiency indicates that the sorting process is reliable and accurate.
- **Total misclassification** metric provides the sum of incorrectly predicted and incorrectly sorted embryos. It offers insight into the overall shortcomings of the system in terms of prediction and sorting, indicating areas for improvement.

Table 3 summarises the results of the zebrafish embryo sorting experiments. The dataset under consideration comprises 622 embryos, which have been categorised into three distinct groups, namely *Stage 1* (n = 160), *Advanced* (n = 256), and *Dead* (n = 206). This distribution is indicative of the extremely rapid developmental dynamics of zebrafish embryos. It should be noted that the duration of *Stage 1* in zebrafish embryos is less than 45 minutes after fertilisation, a period that is under-represented in collected samples. This is primarily attributable to the time between the collection at the zebrafish facilities and the experimental location of this setup, despite the implementation of continuous flow capture conditions during the sorting method. While *Stage 1* is the most annotated class in the training dataset, it exhibits the lowest classification accuracy (90.63 %) and sorting efficiency (88.13 %). This underperformance does not stem from limited representation, but rather reflects a directional misclassification tendency, with a substantial number of *Advanced* embryos being predicted as *Stage 1*. This attitude of the model is perceptible in the confusion matrix where it is clear that the advanced stages are sometimes confused with the *Stage 1* (See the confusion matrix in **Supplementary Figure S7**). The primary source of these detection errors is the morphological similarity between *Stage 1* and *Advanced* embryos, particularly around 2.25 hours post-fertilisation. During this developmental window, overlapping visual characteristics emerge, especially in phases of early cell division, where blastomere symmetry, yolk opacity, and cell boundary contrast are not clearly distinguishable. Consequently, the model is unable to establish a reliable boundary in feature space, and less distinct *Advanced* embryos are frequently projected into the outlet corresponding to *Stage 1*. Despite achieving a relatively high classification accuracy of 93.83 %, the

Parameters	Stage 1	Advanced	Dead
Correctly predicted	145	239	204
Incorrectly predicted	15	17	2
Correctly sorted	141	235	199
Incorrectly sorted	4	4	5
Total embryos	160	256	206
Accuracy (%)	90.63	93.83	98.96
Sorting eff. (%)	88.13	91.41	96.61
Total misclassification	19	21	7

Table 3. Embryo prediction and sorting statistics during experiments.

Advanced class accounts for the highest number of misclassifications (n = 21). This is partly due to the high number of *Advanced* embryo used in experiments but also reflects its transitional morphology, which increases the likelihood of overlap with both *Stage 1* and *Dead* classes. The confusion between *Advanced* and *Dead* is less prominent, indicating that the boundary between viable and non-viable phenotypes is better defined. The *Dead* class exhibits the most robust performance, with 98.96 % classification accuracy and 96.61 % sorting efficiency. Its distinctiveness in terms of phenotype enables effective separation in the feature space, and the minimal discrepancy between classification and sorting outcomes (n = 5) validates the mechanical consistency of the downstream system. In general, the efficiency of sorting is closely related to the accuracy of classification, suggesting that prediction is the bottleneck step in the pipeline. The substandard performance observed in *Stage 1*, despite the provision of extensive annotation, suggests the presence of a representation bottleneck, indicating the model's inability to encode fine-grained early-stage morphological cues effectively. Addressing this issue will likely require the refinement of training strategies, and potentially the incorporation of temporal information to contextualize static morphological ambiguity. This is particularly salient in the context of zebrafish, where *Stage 1* is rapidly surpassed within 45 minutes post-fertilization, further complicating the task of consistent early-stage detection.

Discussion

Given that the majority of zebrafish embryo sorting systems reported in the literature are automated and utilise robotics Diouf et al.[34], Breitwieser et al.[35], Graf et al.[22], an investigation is carried out into the potential of sorting embryos using a microfluidic chip. This system eliminates the labor-intensive tasks typically performed by biologists in laboratory settings while offering a superior methodology for embryo viability through microfluidics. It enables noninvasive, precise sorting of embryos with controlled fluid flow, minimizing damage and cross-contamination. In order to address these considerations, a microfluidic chip has been designed on the basis of bifurcation laws, and is equipped with six channels, three inlets (S0, S1, S2) and three outlets (S3, S4, S5). However, instances of flow irregularities during experiments occasionally resulted in sorting errors. These are likely caused by transient flow disturbances or inconsistencies in the pressure gradients. The implementation of real-time flow monitoring and feedback control could serve to mitigate these issues. Additionally, future CFD models could incorporate variations in embryo size and density in order to simulate real-world conditions with greater accuracy, thereby improving sorting reliability.

The Table 4 provides a comparative analysis of embryo sorting and detection across different studies, highlighting the strengths and unique aspects of our current work. In terms of sample size, this study employed a total of 622 embryos for sorting experiments, which is less than the 4752 and 694 embryos used in the aforementioned studies. The discrepancy in sample size may impact the reliability of our findings, as larger samples can facilitate more comprehensive data collection. The results presented herein demonstrate the capacity to classify embryos across developmental stages, thereby addressing a limitation of previous studies in this field. To illustrate, the methodology proposed by Breitwieser et al.[35] is concerned with the differentiation of rx3 embryos from non-rx3 embryos (including wild-type embryos, empty chorions, and coagulated eggs), but it does not consider the specific developmental stages involved. In contrast, the approach outlined by Graf et al.[22] is limited to the classification of embryos as either fertilised or unfertilised, damaged, or healthy. Although the system demonstrates encouraging results in the classification of embryos into developmental stages, there is scope for further improvement, particularly in the case of *Stage 1* and *Advanced* classes. The particularly high accuracy for the *Dead* class (99.03 %) is crucial for contamination prevention, as the removal of non-viable embryos is a primary objective in sorting workflows. The sorting of embryos at specific developmental stages is of pivotal importance in achieving synchronised samples. Synchronisation is of critical importance for accurate and reproducible comparisons in developmental biology, particularly in studies focusing on gene expression and organ formation. By ensuring that all embryos within a sample are at the same stage of development, researchers can minimise variability and improve the precision of downstream analyses. This capability allows for highly controlled experimental conditions, enabling deeper insights into stage-specific developmental processes, molecular pathways, and their implications for embryogenesis.

Tasks/Methods	Diouf et al.[34]	This work	Breitwieser et al.[35]	Graf et al.[22]
Num. of embryos	320	**622**	4752	694
Embryo sorting efficiency	97.9%	$Stage\ 1$: **88.13%** *Advanced*: **91.80%** *Dead*: **96.60%**	-	96.8%
Embryo prediction accuracy	-	$Stage\ 1$: **90.63%** *Advanced*: **93.36%** *Dead*: **99.03%**	-	-
Sorting speed (per 1 embryo)	3 s	$<$**3 s**	14 s	8 s
Detection speed (per 1 embryo)	10.6 ms	**10.5 ms**	1 s	-
Embryo detection method	YOLOv5	**YOLOv8**	Template-matching	CNN
Sorting device	Robotic	**On-chip, microfluidic**	Robotic	Millifluidic
Invasiveness	Invasive	**Noninvasive**	Invasive	Noninvasive

Table 4. Comparison of our work with the literature.

The system achieves an average sorting speed time of 2.92 s per embryo, which compares favorably to other reported methods in the literature, including rates of 3 s for Diouf et al.[34], 14 s for Breitwieser et al.[35], and 8 s for Graf et al.[22] per embryo. This improvement is attributable to our microfluidic design, which employs a dedicated channel for each class. By directing the flow of embryos in a single step to their respective sorting channels, the necessity of complex, multistep robotic processes is eliminated. This average sorting time (2.92 s) indicates that sorting occurs within the biomechanical safety zone illustrated in Fig. 3d, thereby ensuring controlled shear stress exposure. This duration is indicative of an effective compromise between embryo safety and operational efficiency, avoiding both excessive stress and overly slow sorting.

These results highlight the efficacy of our approach, offering a reliable and efficient solution for embryo sorting while maintaining high accuracy and speed across diverse developmental stages. In our previous approach[34], it was necessary to perform a pick-and-place operation to sort the embryos. In contrast, the new method is much more straightforward and also faster. Given the accelerated progression of these stages, the capacity to rapidly distinguish, categorise and sort embryos at different developmental stages is crucial. In some instances, a specific developmental stage of the embryo is of particular importance, as exemplified by microinjection, typically conducted at the one-cell stage (*Stage 1*). Moreover, our embryo detection speed of 10.5 ms per embryo is significantly faster than the 1-second detection time reported in[35], highlighting the efficiency of our approach. Our system employs a DL approach utilising the YOLOv8 algorithm, which offers superior computational efficiency and real-time object detection capabilities. In contrast to conventional convolutional neural network (CNN) architectures or template matching techniques, YOLO processes the entire image in a single pass, treating object detection as a unified regression problem. It uses a grid-based approach to predict bounding boxes and classes simultaneously, eliminating the need for separate region proposals. Its lightweight architecture and parallel predictions maximize computational efficiency. This enables the system to process data effectively, particularly in scenarios involving zebrafish embryos passing through a microfluidic environment.

The system's automation is achieved through microfluidic technology, as opposed to the use of robotic mechanisms, which are commonly utilised in analogous applications. The manipulation and analysis of samples at the microscale level can be streamlined through the use of microfluidics, which provides precise control over fluid flow at this level. This option not only reduces the overall system cost by minimising mechanical complexity but also improves scalability and accessibility, rendering it suitable for a wide range of research and clinical applications. One of the key distinguishing features of our approach is its noninvasive nature. In contrast to many comparable systems, which rely on invasive methods such as mechanical (Diouf et al.[34], Breitwieser et al.[35]) or optical manipulation[32], the microfluidic-based system preserves the structural and functional integrity of embryos throughout the process. Using noninvasive techniques is critical for maintaining embryo viability, as they mitigate the risks of stress or damage induced by physical contact or external forces. The system utilises a gentle, laminar flow to guarantee exact handling, thereby minimising stress and preventing physical damage to biological samples. This precision enables the safe and effective manipulation of fragile samples, thus preserving their integrity for developmental, toxicological, and biomedical research. This preservation directly contributes to improved outcomes regarding efficiency, accuracy, and overall sample quality. It is acknowledged, however, that future work should include a quantitative assessment of post-sorting viability and stress markers in order to further validate the biological safety of the platform.

The YOLOv8-based microfluidic sorter achieved a sorting efficiency of 88.13% for *Stage 1* zebrafish embryos. In contrast, the COPAS XL system, which uses time-of-flight and optical density detection, reported a sorting accuracy of 99.4 % and a purity of 98.8 % for 10–14 hours post fertilization zebrafish embryos[47]. The BioSorter shows similar performance, with reported efficiencies typically in the $98--99\%$ range under optimized fluorescent labeling[33]. From a financial perspective, our entire hardware setup costs 3,880 - 5,615€as illustrated in Table 5. In contrast, commercial platforms such as COPAS and BioSorter require notable investments, for instance, COPAS systems typically integrate four lasers, each costing approximately 5,000 - 15,000€. Therefore, a single laser module can exceed the total cost of our entire system, without even accounting for the remaining hardware, optics, or software. Furthermore, the system supports label-free, image-based sorting that can use using retrainable AI, and is modular and can be scalable through channel duplication or model updates. While COPAS and BioSorter excel in speed and purity, their dependency on fluorescence detection and rigid proprietary components significantly limits adaptability to morphology-based or unlabeled biological applications. Also,

Component	Model/Description	Estimated Cost (euros)
Microfluidic chip fabrication	PDMS casting + mold prototyping (1–2 devices)	50-100
Pumps (P0 to P5)	Kamoer X1 NKCP-S10B and X5 NKCP-S04B (12V peristaltic)	360-480
Motor driver circuit	L293D motor shield + wiring	10-20
Microcontroller	ATmega328p (Arduino-compatible)	10-15
Industrial camera	IDS UI–3590CP-C-HQ (5 MP CMOS)	600-900
Digital microscope	Dino-Lite AM7915MZTL (long WD, polarizer)	2,000-3,000
Computer workstation	ASUS ROG G752VS (i7–6700HQ, 12 GB RAM, GTX 1070)	800-1,000
Misc. (tubing, connectors, reservoirs)	Silicone tubing, 3D-printed holders, fittings	50-100
Software	YOLOv8 (open-source, local inference)	0
Total Estimated Cost		**€3,880-5,615 €**

Table 5. Estimated cost breakdown of the microfluidic embryo sorting system.

the system has been designed to accommodate specimens measuring between 0.5 and 2 mm, rendering it an appropriate choice for delicate organisms such as medaka (0.5 mm) and Xenopus laevis embryos (1 - 1.2 mm). The microfluidic system has been designed to accommodate specimens measuring between 0.5 and 2 mm, rendering it an appropriate choice for the delicate organisms such as medaka (0.5 mm) or Xenopus laevis embryos (1 - 1.2 mm). Integrating high-speed deep learning algorithms with cost-effective and noninvasive microfluidic systems allows for a unique balance of performance, affordability, and biological safety. This combination positions the system as a robust solution for applications requiring precise, rapid, and reliable cell or embryo analysis.

However, our research has various limitations; an analysis of the results of the misclassification balance (see Table 3) indicates that while the sorting method achieves favorable performance, the detection model exhibits notable deficiencies, particularly for the *Advanced* and *Stage 1* classes. It demonstrates that the number of incorrectly predicted instances is nearly double that of incorrectly sorted instances for these stages. This discrepancy highlights a deficiency in the accuracy of the detection process, which has a cascading effect on the sorting process and identifies key areas for improvement within the detection model. The main source of these detection errors is the morphological similarity between embryos in the *Advanced* (especially at 2.25 hpf) and *Stage 1* stages of development. In many instances, these developmental stages display overlapping visual characteristics, particularly during specific phases of cell division, which presents a significant challenge to accurate differentiation. To address this issue, it would be necessary to integrate a higher resolution imaging system, capable of providing the level of detail required to differentiate subtle features. A promising approach would be to enhance the detection model with temporal context by incorporating time-series image data as opposed to relying solely on static images. By analysing morphological changes over a brief time period, the model is capable of acquiring developmental trajectories of embryos, thereby enhancing the accuracy of stage differentiation. Furthermore, the implementation of attention-based architectures (e.g., Transformers or attention modules within CNNs) has the potential to enable the model to focus on subtle yet critical visual cues that differentiate between similar stages. The augmentation of the training dataset with synthetic images or annotated time-lapse sequences has the potential to enhance the model's robustness to intra-stage variability. The enhancement of detection accuracy, in particular for the *Advanced* and *Stage 1* classes, would have the potential to significantly improve the overall performance of the system. By reducing classification errors, the precision of the sorting process could be further optimised, resulting in more synchronised samples and greater reliability in downstream analyses. Embryos that do not achieve optimal sorting are typically the result of inadequate separation, transient flow blockages, or insufficient water levels within the microfluidic chip. It is important to note that these issues are not a result of deficiencies in the sorting algorithm or methodology, which is performing as designed.

A significant challenge arises from the buoyancy of embryos within the fluidic environment, which can result in overturning and subsequent obscuration of key developmental stage markers. This can impede the accuracy of detection, as the orientation of the embryo is of critical importance in correctly identifying its stage of development. To address this challenge, two potential solutions are proposed for future investigation: **the deployment of two cameras**, one positioned above and the other below the microfluidic chip, could facilitate the capture of complementary views of the embryos, thereby ensuring the visibility of critical morphological features regardless of their orientation. **Rotational Fluid Dynamics**, the implementation of a method to gently rotate the embryos within the fluid would allow all sides of the embryos to be visible during the detection process, effectively eliminating errors caused by obscured features. Both approaches can potentially enhance detection robustness by compensating for embryo buoyancy and orientation, leading to improved sorting accuracy and system reliability.

The present study proposes a cost-effective, efficient, and accurate embryo sorting method, with faster sorting and detection speeds compared to existing robotic systems. Although our microfluidic approach is invasive, this compromise enables us to provide a cost-effective solution. Further testing with larger sample sizes could assist in refining the accuracy and validating the broader applicability of the system. Scaling beyond lab prototypes can be achieved by combining parallel microfluidic channels with multi-camera setups, allowing simultaneous processing and imaging of multiple embryos while maintaining resolution and leveraging low-cost hardware like Raspberry Pi for affordability. The modular system could support AI-driven classification, integration with microinjection and sorting devices, and automated data export, making it a scalable and practical solution ready for real-world deployment.

Methods

Experimental devices

The core of the experimental setup is the microfluidic chip, detailed in **Supplementary Material in Section S1: Chip design and fabrication, Figure S1**, which serves as the primary tool for embryo manipulation and sorting. The system is constructed around a multi-pump fluidic configuration, enabling precise regulation of flow rates. The primary pump (P0) is a *Kamoer NKCP-S10B 12V* peristaltic pump, which is commonly employed in aquarium applications and capable of delivering flow rates ranging from 19 to 65 milliliters per minute. The system is further augmented by five additional pumps (P1 to P5), which are of the same peristaltic type as the main pump, but are designed for lower flow applications, with adjustable output between 4 and 14 millilitres per minute. These pumps ensure versatile and accurate fluid handling depending on the experimental requirements. The system is controlled by a high-performance PC, an *ASUS ROG G752VS* laptop, which is equipped with an *Intel Core i7–6700HQ processor*, *12 GB of RAM*, and a *NVIDIA GeForce GTX 1070* graphics card. This supports both real-time processing and deep learning inference tasks. The central control unit is based on an *ATmega 328p* microcontroller, a reliable and widely used chip for embedded control, which is responsible for orchestrating the actuation of the pumps and interfacing with other components. The peristaltic motors are managed by a pump driver circuit based on a *L293D motor shield*, ensuring proper voltage and current delivery for motor operation.

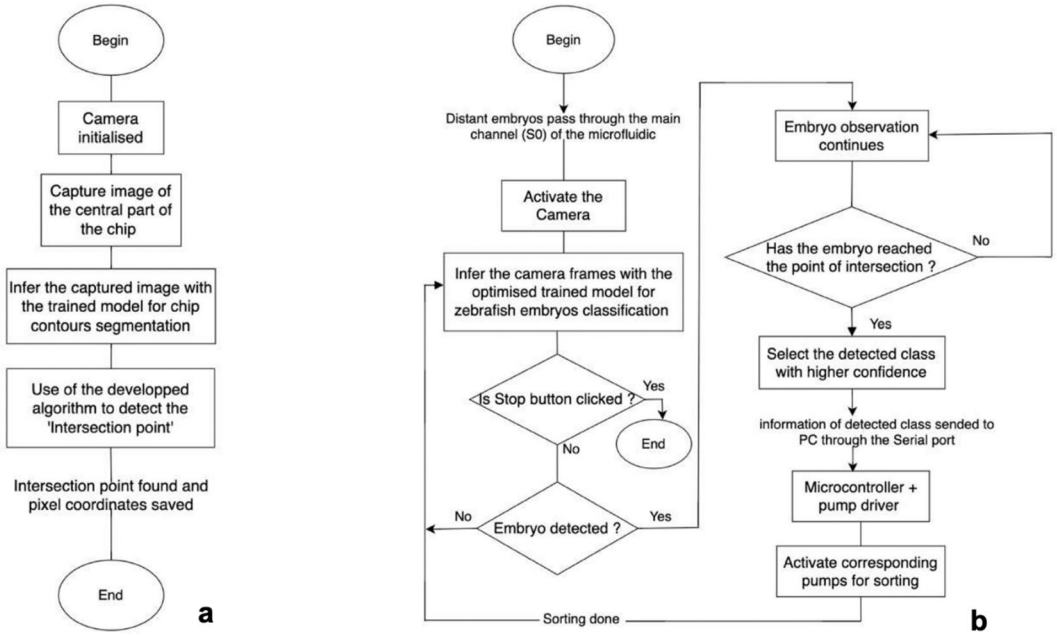

Fig. 8. Initial stages of the system's operation (**a**)*Intersection point* search flow diagram. (**b**) Embryo classification and information transmission flow diagram.

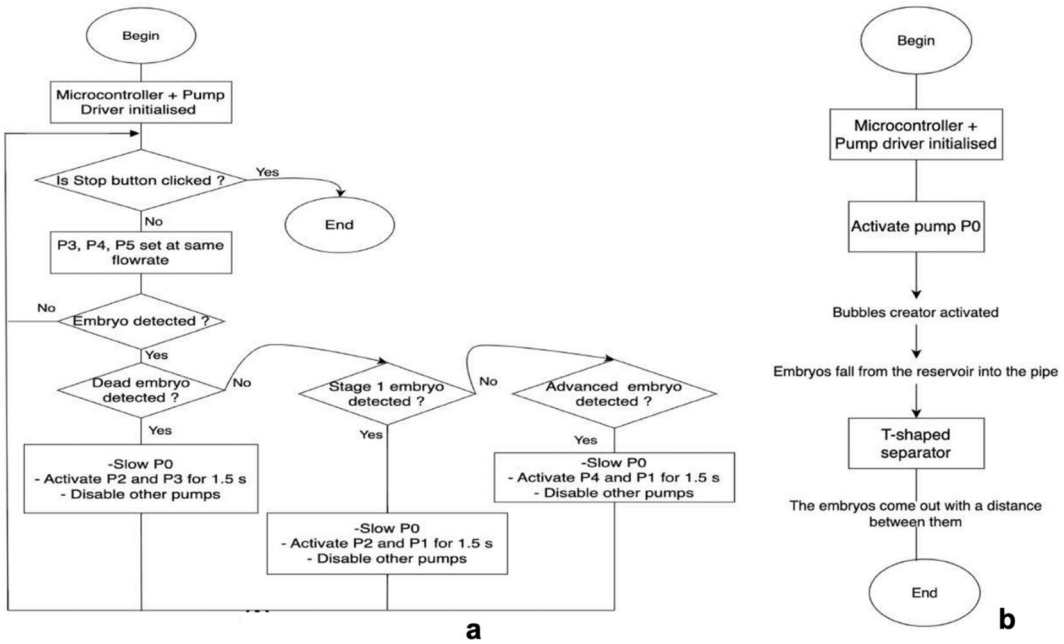

Fig. 9. Subsequent stages of the system's operation, focusing on the control and sorting processes. (**a**) Pump control flow diagram Based on embryo classification (**b**) Embryo release and separation flow chart with T-shaped Separator.

The acquisition of visual data is facilitated by an industrial camera (*UI–3590CP-C-HQ*, from IDS Imaging Development Systems), which provides high-quality imagery, a prerequisite for subsequent analysis. Two types of microscopy solutions are available for optical inspection, depending on the task: a *NIKON SMZ800N* stereo microscope and a *Dino Lite AM7915MZTL* digital microscope, allowing for flexible magnification and imaging conditions. Finally, the system leverages the power of deep learning for object detection and classification, employing the YOLOv8 model, a state-of-the-art object detection framework that is renowned for its accuracy and speed.

Operational workflow of the proposed system

The flowcharts presented in Figs. 8 and 9 illustrate the operational workflow of the system. This process integrates multiple components, including microcontrollers, a microfluidic chip, a fluidic system, pumps, a microscope, and deep learning algorithms, to regulate and monitor the passage of embryos within a controlled flow environment. Each figure outlines specific stages of the process. Figure 8a depicts with the detection of the *Intersection point*, a critical reference point in the flow environment. Figure 9b details the embryo release and separation process, employing a T-shaped separator to streamline this step. Next, Fig. 8b depicts the embryo classification and information transmission process, where deep learning algorithms analyze the embryo and communicate the classification results. Finally, Fig. 9a presents the pump control flow diagram, which adjusts the fluidic system based on the classification, ensuring accurate and efficient embryo sorting.

Figure 8a depicts the initial stage of the process, which commences with the initialisation of the camera. This is followed by the capture of an image of the central region of the chip. Subsequently, the image is processed with a trained model in order to segment the contours of the chip. Subsequently, an algorithm developed in this study is employed to identify the *Intersection point*. Once the point in question has been identified, its corresponding pixel coordinates are stored, thereby concluding this process. Following the initialisation of the microcontroller and the pump driver, the program initiates the activation of pump P0, which in turn activates the bubble creator (see Fig. 9b). The system releases the embryos from the reservoir into a pipe, where they pass through a T-shaped separator. The T-shaped separator is designed to ensure that the embryos emerge from the system with a distance between them before reaching the microfluidic chip. The camera is activated for observation of the zebrafish embryos. The frames are processed with an optimised trained model that is specifically designed for the classification of zebrafish embryos. The programme incorporates a verification process for the stop button, which, if selected, initiates the termination of the current operation. Should the process continue, a further check is made for the detection of the embryo. In the absence of an embryo, the system resumes observation. Conversely, upon the detection of an embryo, the system determines whether it has reached the point of intersection (see Fig. 8b). Upon reaching this point, the embryo class with the highest confidence is selected. Given that embryos often rotate within the liquid stream and may temporarily obscure morphological cues, the system performs multi-frame object detection and retains the class with the highest confidence prior to the sorting junction. The selected class is defined as:

$$\hat{y} = \arg\max_{c \in \mathcal{C}} \left(\max_{t < t_{\text{int}}} \text{Conf}_t^{(c)} \right) \tag{10}$$

where: $\mathcal{C}$ is the set of all possible embryo classes (e.g., *Dead*, *Advanced*, *Stage 1*), $\text{Conf}_t^{(c)}$ is the confidence score of class c at time t, t_{int} is the estimated time at which the embryo reaches the intersection point. Once the detection is confirmed, a segmentation process extracts the embryo's position in the image frame. The embryo's centroid coordinates $(x_{\text{emb}}, y_{\text{emb}})$ are computed from the binary segmentation mask using spatial moments:

$$(x_{\text{emb}}, y_{\text{emb}}) = \left(\frac{M_{10}}{M_{00}}, \frac{M_{01}}{M_{00}} \right) \tag{11}$$

where M_{ij} are the raw moments of the binary image.

In parallel, the coordinates of the closest microchannel intersection point $(x_{\text{int}}, y_{\text{int}})$ which are precomputed through the developed methodology. The embryo-to-*Intersection point* pixel distance is calculated with :

$$D(t) = \sqrt{(x_{\text{emb}}(t) - x_{\text{int}})^2 + (y_{\text{emb}}(t) - y_{\text{int}})^2} \tag{12}$$

A decision threshold δ in is defined such that when the embryo reaches a proximity satisfying $D(t) \leq \delta$.

Once this condition is reached, the selected class $\hat{y}$ (Equation 10) information is then transmitted to a PC via the serial port to the microcontroller. The microcontroller and pump driver are subsequently activated to trigger the appropriate pumps for embryo sorting based on the detected class. In the absence of embryo detection, pumps P3, P4, and P5 are configured to operate at a uniform flow rate. In the event of a dead embryo, pump P0 is decelerated, pumps P2 and P3 are engaged for 1.5 s, and all other pumps are deactivated. This temporal parameter is determined through the execution of experiments on the microfluidic chip, with the objective of ascertaining the minimum time required for the efficient sorting of embryos within the dimensions of the chip in use. In the event that the embryo is viable, a determination is made as to whether it is in stage 1 or an advanced stage. In the case of a stage 1 embryo, the flow rate of pump P0 is reduced, while pumps P2 and P1 are activated for a period of 1.5 s, and all other pumps are deactivated. In the event that the embryo is in an advanced stage of development, the flow rate of pump P0 is reduced, while pumps P4 and P1 are activated for a period of 1.5 s, and all other pumps are deactivated (see Fig. 9a).

Data collection and labelling

A database of images from our previous work[48] is combined with a new set, resulting in a total of 1366 images of zebrafish embryos. Wild-type adult zebrafish are maintained according to the standard protocol[49] in the Animal Facility and Engineering Aquatic Models Platform of Sorbonne University. Embryos used in this study are collected through natural spawning on the day of each experiment from the same facility. Zebrafish are renowned for their prolific embryo production, with the embryos typically collected shortly after spawning. After collection, the embryos are incubated in E3 solution. It refers to a commonly used growth medium specifically designed for maintaining zebrafish embryos at the developmental stage around 3 days post-fertilization. This medium

(34.8 g NaCl, 1.6 g KCl, 5.8 g $CaCl_2.H_2O$, 9.78 g $MgCl_2.6H_2O$) is crucial for providing the necessary nutrients, ions, and environmental conditions to support embryonic development and viability. The images are classified into three classes: *Stage 1*, *Dead* and *Advanced* stage. The data are split into training, validation, and testing sets using a ratio of 70:20:10, respectively. *RoboFlow*[50] tool is used to prepare the dataset. The bounding box tool is used for annotating images. The dataset under consideration contains an imbalanced class distribution across 3120 annotations. *Stage 1* is the most prevalent class, with 1,258 annotations (889 train, 257 validation, 112 test), followed by *Advanced* stage with 1,048 annotations (758/181/109). The *Dead* class is the least represented, with a total of 714 annotations (599/163/52), and is especially underrepresented in the test set (52 out of 273). Refer to **Supplementary material Section S5 : Zebrafish embryo dataset for model training, Figure S5, Figure S6 and Table S3** for further details about the basic dataset.

In order to enhance the generalisation and robustness of the model when operating under realistic imaging conditions, a data augmentation procedure is implemented that involved the application of horizontal flipping and random rotations within $\pm 15^{\circ}$. These transformations are well-suited for zebrafish embryos transiting through microfluidic channels, where slight orientation changes and lateral flips occur due to flow dynamics. The augmentations simulate natural variability without compromising morphological integrity, thereby enhancing the model's capacity to detect embryos despite minor misalignments or pose variations introduced by the imaging system or fluidic motion. Following the augmentation steps of the dataset, a total of 3481 images are obtained with 7950 annotations.

Description and evaluation of YOLOv8 algorithm

The YOLO (*You Only Look Once*) model has made significant strides in the field of computer vision, representing a notable success. Developed by the *Ultralytics company*[51], it has gained widespread recognition. YOLOv8 boasts improved detection accuracy and speed, making it a leading choice for various applications in computer vision. This version of YOLO is employed for training purposes. The architecture builds upon YOLOv5's backbone with the introduction of the C2f module, replacing C3, to enhance gradient flow while maintaining a lightweight design. In YOLOv8, the loss consists of two parts: classification branch, which utilizes Binary Cross Entropy (BCE) Loss, and regression branch, responsible for bounding box prediction, which uses a combination of two independent losses: Distribution Focal Loss (DFL) and Complete Intersection over Union (CIoU) loss.

$$\mathrm{Loss}_{\mathrm{YOLOv8}} = \mathrm{Loss}_{\mathrm{BCE}} + \mathrm{Loss}_{\mathrm{DFL}} + \mathrm{Loss}_{\mathrm{CIoU}} \tag{13}$$

Common evaluation metrics for DL are precision (P), which is precision rate, recall rate (R) and mean average precision (mAP). The expressions of P and R are as follows:

$$P = \frac{TP}{(TP + FP)} \tag{14}$$

$$R = \frac{TP}{(TP + FN)} \tag{15}$$

Among them, true positives (TP), false positives (FP), and false negatives (FN), represent positive samples with correct classification, negative samples with incorrect classification, and positive samples with incorrect classification, respectively. So Equation 14 measures how many of the items identified as relevant are actually relevant, while Equation 15 measures how many of the truly relevant items were successfully identified. AP is the average accuracy rate, which is the integral of the P index to the R index; mAP is the average accuracy of the mean, which means that the AP value of each category is summed, and then divided by all categories, i.e., the average value. It is defined as follows:

$$mAP = \frac{1}{|Q_R|} \sum_{q=Q_R} AP(q) \tag{16}$$

A high *mAP* means that the model has both a low false negative rate and a low false positive rate. The higher the *mAP*, the more precise and the higher the recall is for the model. Furthermore, *mAP* is available in a variety of forms, each tailored to a specific Intersection over Union (IoU) threshold. For instance, *mAP@0.5* is designed to focus on an IoU threshold of 0.5, while *mAP@0.50:0.95* encompasses the mean average precision over a spectrum of IoU thresholds ranging from 0.5 to 0.95.The harmonisation of the average between precision and recall is called the $f1 - score$.

$$f1 - score = \frac{2 \times P \times R}{P + R} \tag{17}$$

A model demonstrating high performance is achieved following a process that involves multiple steps. Hyperparameter tuning in object detection is the process of selecting the optimal values for parameters that shape the model's architecture and training process. These parameters exert a significant influence on the model's accuracy, precision, and recall. The process of hyperparameter tuning involves the systematic testing of different parameter combinations with the objective of identifying the configuration that maximises the chosen performance metric, such as accuracy or *mAP*. The basic loss function of YOLOv8 has not been altered. Instead, a genetic algorithm is applied to optimize the YOLO hyperparameters after using the classic YOLO loss function. Models are selected based on a fitness score derived from the evaluation metrics, aiming to maximize this score.

The goal is to maximise fitness (see Equation 18). YOLOv8 has a default fitness function which is a weighted combination of metrics *mAP* contributes 10 % of the weight and *mAP@0.5:0.95* contributes the remaining 90 %. The default fitness function is utilised, which is defined as follows:

$$\text{fitness} = w_1.P + w_2.R + w_3.mAP@0.5 + w_4.mAP@0.5:0.95 \tag{18}$$

where: *P* represents Precision, *R* represents Recall, *mAP* represents mean Average Precision at 0.5, *mAP@0.5:0.95* represents mean Average Precision from 0.5 to 0.95, w_1, w_2, w_3, w_4 represent the corresponding weights defined as [0.0, 0.0, 0.1, 0.9]. These models are then subjected to a genetic algorithm mutation operator, which introduced random perturbations to explore new configurations while preserving successful solutions. The utilisation of genetic algorithms enables the optimisation process to investigate a diverse array of hyperparameter configurations, thereby facilitating the identification of superior solutions in comparison to traditional methodologies such as grid search or random search. The stochastic nature of genetic algorithms enables the escape from local minima, thus facilitating the discovery of robust hyperparameter combinations that enhance the performance of the YOLOv8 model. The initial step involves the generation of a population of hyperparameter candidates, which are set as the default YOLOv8 hyperparameters. Each candidate represents a distinct combination of hyperparameter values. Subsequently, each candidate is evaluated in accordance with the specified fitness function, as expressed by Equation 18. Subsequently, the candidates are selected for reproduction, with those demonstrating superior performance having a higher probability of being chosen. The selected candidates then undergo crossover, whereby aspects of two parent candidates are combined, and mutation, whereby some hyperparameters are randomly altered to introduce variability. The new generation of candidates then replaces the old one, and this process continues for a predetermined number of generations. This iterative approach effectively explores the hyperparameter space, with the potential to improve model performance and generalisation in YOLOv8. Subsequently, the generation of hyperparameters that attains the highest fitness score is selected.

Computational Fluid Dynamics (CFD) modelling

In order to gain a more accurate understanding of the system in question it is necessary to establish a model that is as close as possible to the reality of the situation. CFD simulations are conducted using *Comsol Multiphysics software*. The Reynolds number is calculated in order to determine the flow nature, which is defined as the ratio of inertial and viscous forces..

$$Re = \frac{\rho.V.L}{\mu} or \frac{V.L}{v} \tag{19}$$

where *Re* is the Reynolds number, ρ is the density of the fluid, *V* is the velocity of the fluid flow, *L* is the lenght, μ is the viscosity of the fluid and v is the kinematic viscosity of the fluid. Using Equation 19, the Reynolds number of 59 is obtained when the maximum flow rate of the micropumps (5000 μ l/min) and water kinematic viscosity at $25°C$. Therefore, the simulations utilized the laminar flow physics module from the CFD module. For an incompressible fluid under laminar flow regime that follows the Navier-Stokes equation, the governing equations determine the pressure and flow velocity as follows.

$$\rho_f.\frac{\partial U}{\partial t} = \nabla.[-pI + \mu(\partial U + (\partial U)^T)] \tag{20}$$

$$\nabla.U = 0(\text{Incompressible flow}) \tag{21}$$

where ρ_f is fluid density, μ is dynamic viscosity, *t* is time, *U* is fluid velocity, *p* is applied pressure, and *I* is identity tensor. Equation 20 represents the stationary step to generate the velocity profile along the channel. The motion of particles in a fluid follows Newton's second law :

$$m_p.\frac{dv_p}{dt} = F_D + F_g + F_{ext} \tag{22}$$

where F_D is the drag force, v_p is particle velocity, m_p is particle mass, F_D, F_g, and F_{ext} are the drag, gravity, and other forces, respectively. When the fluid flows sideways to the force of gravity, known as transverse flow, the way it focuses remains unaffected when water is the sample fluid. The Schiller-Naumann drag law is applicable over a moderate range of relative Reynolds number $R_{e_r} < 800$. The governing equation for particle tracing is expressed as follows:

$$\begin{aligned} F_D &= \frac{1}{\tau_p}.m_p(U - v_p) \\ with \tau_p &= \frac{4\rho_p d_p^2}{3\mu C_D R_{e_r}}, \\ C_D &= \frac{24}{R_{e_r}}(1 + 0.15R_{e_r}^{0.687}), \\ R_{e_r} &= \frac{\rho|U - v_p|d_p}{\mu} \end{aligned} \tag{23}$$

where F_D is the drag force, v_p is particle velocity, m_p is particle mass, ρ_p is particle density, and d_p is particle diameter, R_{e_r} the relative Reynolds number, ρ density of the fluid and μ dynamic viscosity of the fluid. Constant volume flow rate boundary condition is used at the sample inlet. Particle motion is elucidated through the application of drag force acting on the particles using Equation 23.

Data availability

The codes for this project, as well as the deep learning models and chip design, can be found in this repository on GitHub: https://github.com/AliouneDiouf/On_Chip_Sorting_Zebrafish_Embryos.git

Received: 22 January 2025; Accepted: 28 August 2025
Published online: 29 October 2025

References

1. Stern, H. M. & Zon, L. I. Cancer genetics and drug discovery in the zebrafish. *Nat. Rev. Cancer* **3**, 533–539 (2003).
2. Chakraborty, C., Hsu, C. H., Wen, Z. H., Lin, C. S. & Agoramoorthy, G. Zebrafish: a complete animal model for in vivo drug discovery and development. *Curr. drug metabolism* **10**, 116–124 (2009).
3. MacRae, C. A. & Peterson, R. T. Zebrafish as tools for drug discovery. *Nat. reviews Drug discovery* **14**, 721–731 (2015).
4. Cassar, S. et al. Use of zebrafish in drug discovery toxicology. *Chem. research toxicology* **33**, 95–118 (2019).
5. Stosik, M., Tokarz-Deptuła, B. & Deptuła, W. Haematopoiesis in zebrafish (danio rerio). *Front. Immunol.* **13**, (2022).
6. Paik, E. J. & Zon, L. I. Hematopoietic development in the zebrafish. *Int. J. Dev. Biol.* **54**, 1127–1137 (2010).
7. Bournele, D. & Beis, D. Zebrafish models of cardiovascular disease. *Hear. failure reviews* **21**, 803–813 (2016).
8. Asnani, A. & Peterson, R. T. The zebrafish as a tool to identify novel therapies for human cardiovascular disease. *Dis. models & mechanisms* **7**, 763–767 (2014).
9. Lu, S. et al. Generation and application of the zebrafish heg1 mutant as a cardiovascular disease model. *Biomolecules* **10**, 1542 (2020).
10. Sajan, S. A. & colleagues. Insights into alzheimer s disease mechanisms using zebrafish models. *Dis. Model. & Mech.* (2023).
11. Arslan-Ergul, A. *et al.* The aging zebrafish brain as a model for alzheimer s disease. *Front. Cell Dev. Biol.* (2023).
12. Chaturvedi, B. et al. A review on role of zebrafish in huntington s disease. *J. Pharm. Res. Int.* **34**, 9–14 (2022).
13. Bates, G. et al. Zebrafish as a model for huntington's disease: Genetic and molecular insights. *Neurogenetics* **20**, 115–125 (2019).
14. Echeverria, G. V. et al. Zebrafish as an experimental model for huntington's disease: therapeutic insights. *Drug Discov. Today* **26**, 564–574 (2021).
15. Harel, I. & colleagues. A novel chemical-combination screen in zebrafish identifies epigenetic small molecule candidates for the treatment of duchenne muscular dystrophy. *Skeletal Muscle* **13**, 42–56 (2023).
16. Kawahara, G. et al. Using zebrafish to model duchenne muscular dystrophy: Genetic insights and therapeutic advances. *Hum. Mol. Genet.* **23**, 4651–4659 (2020).
17. Zon, L. I. & Peterson, R. T. In vivo drug discovery in the zebrafish. *Nat. reviews Drug discovery* **4**, 35–44 (2005).
18. Bionomous. Zebrafish early embryo sorting (2020). https://bionomous.ch.
19. Meyers, J. R. Zebrafish: development of a vertebrate model organism. *Curr. Protoc. Essent. Lab. Tech.* **16**, (2018).
20. Nasiadka, A. & Clark, M. D. Zebrafish breeding in the laboratory environment. *ILAR J.* **53**, 161–168 (2012).
21. Mohand-Ousaid, A., Haliyo, S., Regnier, S. & Hayward, V. High fidelity force feedback facilitates manual injection in biological samples. *IEEE Robotics and Automation Letters* **5**, 1758–1763 (2020).
22. Graf, S. F. *Automated microinjection with integrated cell sorting, immobilization and collection*. Ph.D. thesis, ETH Zurich (2011).
23. LaBelle, C. A., Massaro, A., Cortés-Llanos, B., Sims, C. E. & Allbritton, N. L. Image-based live cell sorting. *Trends Biotechnol.* **39**, 613–623 (2021).
24. Sadak, F., Saadat, M. & Hajiyavand, A. M. A vision-guided methodology for the automation of biological cell injection. In *2020 2nd International Conference on Electrical, Control and Instrumentation Engineering (ICECIE)*, 1–9 (IEEE, 2020).
25. Cordero-Maldonado, M. L. et al. Deep learning image recognition enables efficient genome editing in zebrafish by automated injections. *PLoS One* **14**, e0202377 (2019).
26. Alegria, A. D. *et al.* A machine vision guided robot for fully automated embryonic microinjection. *bioRxiv* 2023–04 (2023).
27. Jones, R. A., Renshaw, M. J., Barry, D. J. & Smith, J. C. Automated staging of zebrafish embryos using machine learning. *Wellcome Open Res.* **7**, 275 (2023).
28. Čapek, D. *et al.* Embryonet: using deep learning to link embryonic phenotypes to signaling pathways. *Nat. Methods* 1–9 (2023).
29. Shang, S., Long, L., Lin, S. & Cong, F. Automatic zebrafish egg phenotype recognition from bright-field microscopic images using deep convolutional neural network. *Appl. Sci.* **9**, 3362 (2019).
30. Qian, C., Tong, M., Yu, X. & Zhuang, S. Cnn-based visual processing approach for biological sample microinjection systems. *Neurocomputing* **459**, 70–80 (2021).
31. Srivastava, S. et al. Comparative analysis of deep learning image detection algorithms. *J. Big data* **8**, 66 (2021).
32. Union Biometrica. Copas flow cytometers (2020). https://www.unionbio.com/copas/.
33. Union Biometrica. Union biosorter brochure (2020). https://www.unionbio.com/documents/UBIO_BioSorter_Brochure_2020_UPDATE.pdf.
34. Diouf, A. et al. Robotic sorting of zebrafish embryos. *J. Micro Bio Robotics* **20**, 3 (2024).
35. Breitwieser, H., Dickmeis, T., Vogt, M., Ferg, M. & Pylatiuk, C. Fully automated pipetting sorting system for different morphological phenotypes of zebrafish embryos. *SLAS TECHNOLOGY: Transl. Life Sci. Innov.* **23**, 128–133 (2018).
36. Xi, H., Zheng, H., Guo, W., Ga n-Calvo, A. & Ai, Y. Active droplet sorting in microfluidics: A review. *Lab on a Chip* **17**, 751–771 (2017).
37. Sajeesh, P. & Sen, A. K. Particle separation and sorting in microfluidic devices: a review. *Microfluidics and nanofluidics* **17**, 1–52 (2014).
38. Zhang, Y., Zheng, T., Wang, L., Feng, L. & Wang, M. From passive to active sorting in microfluidics: A review. *Rev. on Adv. Mater. Sci.* **60**, 10–28 (2021).
39. Gossett, D., Weaver, W., Mach, A. & Hur, S. Label-free cell separation and sorting in microfluidic systems. *Anal. Bioanal. Chem.* **397**, 3249–3267 (2010).
40. Shen, Y., Yalikun, Y. & Tanaka, Y. Recent advances in microfluidic cell sorting systems. *Sensors and Actuators B: Chem.* **287**, 527–543 (2019).
41. Hu, D., Liu, H., Tian, Y., Li, Z. & Cui, X. Sorting technology for circulating tumor cells based on microfluidics. *ACS Comb. Sci.* **22**, 161–176 (2020).
42. Zhao, Y. et al. A review of automated microinjection of zebrafish embryos. *Micromachines* **10**, 7 (2019).
43. Otterstrom, J. J., Lubin, A., Payne, E. & Paran, Y. Technologies bringing young zebrafish from a niche field to the limelight. *SLAS technology* (2022).
44. Union Biometrica. Biosorter (2020). https://www.unionbio.com/biosorter/.

45. Wyatt Shields IV, C., Reyes, C. D. & L pez, G. P. Microfluidic cell sorting: a review of the advances in the separation of cells from debulking to rare cell isolation. *Lab Chip* **15**, 1230–1249, https://doi.org/10.1039/C4LC01246A (2015).
46. Akagi, J. et al. Miniaturized embryo array for automated trapping, immobilization and microperfusion of zebrafish embryos. *PloS one* **7**, e36630 (2012).
47. Union Biometrica. Copas xl flow cytometers brochure (2008). https://www.unionbio.com/documents/COPASXL_Brochure08-05.pdf.
48. Diouf, A. *et al.* Automatic sorting of zebrafish embryos using deep learning. In *2023 International Conference on Manipulation, Automation and Robotics at Small Scales (MARSS)*, 1–6 (IEEE, 2023).
49. Westerfield, M. The zebrafish book; a guide for the laboratory use of zebrafish (danio rerio). *(No Title)* (2007).
50. Dwyer, B., Nelson, J., Solawetz, J. *et al.* Roboflow (version 1.0)[software]. https://roboflow.com.computervision (2022).
51. Redmon, J., Divvala, S., Girshick, R. & Farhadi, A. You only look once: Unified, real-time object detection. In *2016 IEEE Conference on Computer Vision and Pattern Recognition (CVPR)*, 779–788, https://doi.org/10.1109/CVPR.2016.91 (2016).

Acknowledgements
The authors thank Edouard Manzoni and Marco Amaral, Lois Bernabé technicians for the Animal Facility and Engineering Aquatic Models Platform of Sorbonne University for providing us fresh zebrafish eggs.

Author contributions
All authors have made substantial contributions to the conception and design of the study. Acquisition of images and analysis (AD, SH), labeling images (AD, AM, DZ), development of the deep learning model (FS, AD), automation process workflow (AD, MB, SH, FS), mechanical design (AD, IF, GL, LB, SH) and manufacturing of the microfluidic chip (AD, FF, EG). (AD, FS) wrote the main manuscript text and final approval of the version submitted (all authors).

Funding
This study is funded by the Université franco-italienne (UFI)/Universitá Italo Francese (UIF). An aspect of this study is partially supported by the Republic of Turkey Strategy and Budget Presidency under project number 2021K12–169131/12.

Declarations

Competing interests
The authors declare no conflict of interest.

Additional information
Supplementary Information The online version contains supplementary material available at https://doi.org/10.1038/s41598-025-17946-7.

Correspondence and requests for materials should be addressed to A.D.

Reprints and permissions information is available at www.nature.com/reprints.

Publisher's note Springer Nature remains neutral with regard to jurisdictional claims in published maps and institutional affiliations.

Open Access This article is licensed under a Creative Commons Attribution-NonCommercial-NoDerivatives 4.0 International License, which permits any non-commercial use, sharing, distribution and reproduction in any medium or format, as long as you give appropriate credit to the original author(s) and the source, provide a link to the Creative Commons licence, and indicate if you modified the licensed material. You do not have permission under this licence to share adapted material derived from this article or parts of it. The images or other third party material in this article are included in the article's Creative Commons licence, unless indicated otherwise in a credit line to the material. If material is not included in the article's Creative Commons licence and your intended use is not permitted by statutory regulation or exceeds the permitted use, you will need to obtain permission directly from the copyright holder. To view a copy of this licence, visit http://creativecommons.org/licenses/by-nc-nd/4.0/.

© The Author(s) 2025